Unveiling neoadjuvant chemotherapy-induced immune landscape remodeling and metabolic reprogramming in lung adenocarcinoma by scRNA-sequencing

Yiwei Huang[1]*; Lin Cheng[2*]; Guoshu Bi[1*]; Jiaqi Liang[1*]; Ming Li[1]; Huan Zhang[3]; Guangyao Shan[1]; Zhengyang Hu[1]; Zhencong Chen [1]; Gujie Wu [1]; Zongwu Lin[1]; Wei Jiang[1]; Qun Wang[1]; Junjie Xi [1#]; Cheng Zhan[1#]; Shanye Yin[4.5#]

1. Department of Thoracic Surgery, Zhongshan Hospital, Fudan University, No. 180, Fenglin Road, Shanghai, 200032, China.

2. Regenerative Medicine Institute, School of Medicine, National University of Ireland (NUI), Galway, Ireland.

3. Department of Thoracic Surgery, Sichuan Cancer Hospital, University of Electronic Science and Technology of China, No. 55, Renmin Road, Chengdu, Sichuan, 610041, China.

4. Department of Pathology, Albert Einstein College of Medicine, Bronx, NY 10461, USA.

5. Einstein Pathology Single-cell & Bioinformatics laboratory, Bronx, NY 10461, USA.

* These authors contributed equally to this work.

Correspondence to:C.Z., czhan10@fudan.edu.cn; J.X., xi.junjie@zs-hospital.sh.cn; S.Y., shanye.yin@einsteinmed.edu

Abstract

Neoadjuvant chemotherapy has emerged as a significant therapeutic approach in the management of lung cancer, aiming to improve outcomes through preoperative systemic treatment. However, the mechanisms underlying treatment efficacy and resistance remain largely unknown. In this study, scRNA-seq analysis of tumor samples from nine lung adenocarcinoma (LUAD) patients, including four with surgery alone and five with neoadjuvant chemotherapy, was conducted. Additionally, a series of in vitro and in vivo assays, encompassing flow cytometry, immunofluorescence, seahorse assay, and tumor xenograft models, were employed to validate our findings. A total of 83,622 cells were analyzed, revealing high heterogeneity in cell type composition across different groups. Functional enrichment analysis uncovered significant metabolic reprogramming induced by chemotherapy in both tumor cells and macrophages. Notably, two macrophage subtypes were identified: Anti-mac cells (CD45+CD11b+CD86+) and Pro-mac cells (CD45+CD11b+ARG+), with the proportion of Pro-mac cells significantly increasing in LUAD tissues after neoadjuvant chemotherapy. Pro-mac cells were found to promote tumor growth and angiogenesis while suppressing tumor immunity. Furthermore, analysis of T and B cell remodeling induced by neoadjuvant therapy revealed a more robust immune cytotoxic response against tumor cells. Our investigation illuminates the intricate metabolic reprogramming occurring within the TME of LUAD in response to neoadjuvant chemotherapy. Specifically, our study highlights the discernible impact on the composition and functionality of immune cells, notably macrophages and T cells. These insights not only deepen our understanding of the nuanced interactions within the TME but also open avenues for the development of novel targeted therapeutic interventions for LUAD.

Keywords: Lung adenocarcinoma, Neoadjuvant chemotherapy, phenotype atlas, metabolic reprogramming

Introduction

Lung cancer is the most common cancer among all human tumor types, with more than $1.7x10^6$ new cases worldwide each year. According to the Global Cancer Report data, lung adenocarcinoma (LUAD) accounts for most lung cancers (1). The application of adjuvant or neoadjuvant chemotherapy (NCT) has significantly improved the long-term survival of LUAD patients. At present, for most LUADs that need chemotherapy after being assessed, chemotherapy will be used before and after surgery (2). Chemotherapy drugs, however, are very toxic and are prone to invalid (3). In addition, continued ineffective chemotherapy will lead to the generation of drug-resistant tumor cell clones (4, 5) and a delay in tumor removal. Almost all cancer patients show inherent or acquired drug resistance, leading to treatment failure and unsatisfactory overall survival. Therefore, to accurately develop therapies that can overcome drug resistance, it is essential to understand the alterations in the tumor microenvironment driven by chemotherapy.

Many studies have increasingly proved the tumor microenvironment (TME) to be an essential source of intratumoral heterogeneity (6). This heterogeneity in the TME includes the differences between tumor cells and tumor cells and the differences between various stromal cells and immune cells. Actively exploring the changes of multiple cells in the TME of LUAD after chemotherapy may finally find an excellent way to overcome chemotherapy resistance for LUAD. In this study, we demonstrated the changes in the microenvironment of lung adenocarcinoma with chemotherapy. In particular, we focused on the effect of chemotherapy on the metabolic reprogramming of tumor cells, stromal cells, and immune cells.

Formerly, it was generally believed that consuming glucose in TME by cancer cells may promote nutritional competition, a metabolic mechanism of immunosuppression (7). However, recent studies have shown that tumor-infiltrating immune cells depend on glucose, and immune cells, especially macrophages, consume more glucose than malignant cells. The impaired immune cell metabolism in the tumor microenvironment (TME) helps tumor cells escape immunity (8). The

internal processes of the cells respectively drive immune cells and cancer cells to obtain glucose and glutamine preferentially. It is believed that the selective cellular allocation of these nutrients can be used to develop therapeutic and imaging strategies to enhance or monitor the metabolic processes and activities of specific cell populations in TME (9). Metabolic reprogramming in various cell types in the tumor microenvironment after undergoing chemotherapy may be an essential feature that affects the effect of chemotherapy. Our research fully demonstrated the metabolic reprogramming landscape of tumor cells, stromal cells, and immune cells before and after chemotherapy.

Results

Single-cell transcriptomic profiling from LUAD

A total of nine patients with non-metastatic LUAD underwent lobectomy with curative intent in the Department of Thoracic Surgery, Zhongshan Hospital of Fudan University. Among them, five received three cycles of preoperative neoadjuvant combination chemotherapy with cisplatin plus pemetrexed (defined as NCT group), while others only received surgery (defined as the Control group). Following resection, a malignant lung tumor sample was obtained from each patient, rapidly digested to a single-cell suspension, and analyzed using 10X scRNA-seq (Fig. 1a). After quality control, a total of 83622 cells that met the inclusion criteria were subjected to subsequent analyses, of which 33567 and 50055 cells were derived from the control and NCT groups, respectively (Fig. 1a-c, Fig S1a). Next, we classified cell types through dimensional reduction and unsupervised clustering via the Seurat package.

Based on the SingleR package, CellMarker dataset, and our previous studies (21, 22), we identified cell clusters that could be readily assigned to known cell lineages: epithelial cells (marked by SFTA2 and KRT8), T cells (marked by CD3D and TRBC2), B cells (marked by CD79A and CD19), endothelial cells (marked by EMCN and CXorf36), mast cells (marked by TPSB2 and TPSAB1), macrophages (marked by

116 CD68 and APOE), monocytes (marked by FGL2 and LGALS2), fibroblasts (marked
117 by LUM and DCN), neutrophils (marked by FCGR3B and CMTM2). Meanwhile, the
118 consensus clustering of these cells also exhibited the consistency and homogeneity of
119 the expression profile within each identified cell type (Fig. 1b). For instance, clusters
120 1, 3, 6, 7, and 15, all designated as epithelial cells, were adjacent to each other in the
121 consensus heatmap. This result confirmed the robustness and reliability of our data
122 pre-processing. Detailed distributions of these marker genes in each cluster are
123 depicted in Fig S1.

124 By comparing the composition of different types of cells in each group, we
125 noticed tumor microenvironment heterogeneity: the proportion of cells other than
126 tumor cells, especially immune cells (mainly T and B), was significantly higher in the
127 NCT (Fig. 1e). Therefore, to identify subclusters within each of these nine major cell
128 types, we performed principal component analysis and observed a complex cellular
129 ecosystem containing eight different epithelial subclusters and 43 non-epithelial
130 clusters. Interestingly, the epithelial subclusters, mainly composed of cancer cells,
131 were highly patient-specific, while the immune cell subclusters mostly consisted of
132 cells derived from four or more patients (Fig. 1f). This observation demonstrated the
133 substantial variation and heterogeneity of tumor microenvironment among groups and
134 individuals. Therefore, we further explored these alterations associated with the
135 therapeutic regimen in greater detail for the primary cell types in subsequent analyses.
136

137 **Metabolic reprogramming in lung adenocarcinoma driven by neoadjuvant**
138 **chemotherapy.**

139 Metabolic reprogramming is a hallmark of malignant tumors. Recent studies have
140 also shown that tumors' metabolic characteristics and preferences change during
141 cancer progression (23). In each type of cell derived from the Control and NCT
142 groups, more significantly up-regulated metabolic pathways were enriched in cancer
143 cells, nonmalignant epithelial cells, fibroblasts, and macrophages (Fig. 2a). The
144 enrichment of oxidative phosphorylation, glycolysis, pyruvate metabolism, and

145 tricarboxylic acid cycle depicted a glucose metabolism activity in those four types of
146 cells. By analyzing the activity of the metabolic pathways of cells from different
147 sources, we found that the activity scores of the metabolic pathways of tumor cells
148 and macrophages were significantly higher than those of other types of cells. Notably,
149 the metabolic pathway activity of macrophages and malignant cells increased after
150 chemotherapy (Fig. 2b).
151

152 **Changes in metabolism and gene expression of tumor cells after neoadjuvant**
153 **chemotherapy**

154 To accurately analyze the effect of chemotherapy on the cancer cells, we first re-
155 clustered the epithelial cells, and 12 clusters were identified (Fig. 3a). Copy number
156 variations (CNVs) (Fig S2a) and marker genes were used to accurately separate
157 malignant and nonmalignant epithelial cells in Control and NCT samples. They were
158 finally defined as MalignantSA cells (Marker genes: FOXL2/MET/CD74), Malignant
159 NCT cells (Marker genes: RAC1/MAF/CXCL1), Malignant PD cells, and
160 Nonmalignant cells (Marker genes: ABCA3/SFTPB/LPCAT) (Fig. 3d). These marker
161 genes were further confirmed by immunofluorescence experiments (Fig S2d). We
162 found that the proportion of malignant cells was significantly reduced after
163 chemotherapy (Fig. 3b, c, Fig S2b). Although malignant cells were significantly
164 reduced after chemotherapy, genetic aberrations by CNVs analysis revealed that
165 MalignantNCT cells exhibited significantly higher malignant scores compared to
166 MalignantSA cells (Fig S2a).

167 We then performed trajectory analysis to quantitatively track the reprogramming
168 of epithelial cells from the three groups. Nonmalignant cells evolved in two directions
169 and developed into two clusters of cells (Fig. 3e). In this evolutionary process,
170 glycolysis-related genes (ENO1, LDHB, GAPDH), oxidative phosphorylation-related
171 genes (NDUFA4), mitochondrial repair-related genes (TOMM7), glucose and lipid
172 metabolism regulation genes (S100A16), ATPase activity-related genes (CCT6A),
173 tumor immune regulation-related genes (CCL20, CXCL1, PAEP, PPP1R14B),

hypoxia response regulation genes (CHCHD2), apoptosis regulation genes (MEG3, CEACAM5), mRNA alternative splicing-related genes (LSM5), and Ras-related protein (RAC1, RALA) gradually increased over time in the pseudotime analysis. It was indicated that these genes play an essential role in epithelial cells transforming into tumor cells (Fig. 3f, Fig S2e). Correspondingly, during the process of epithelial cells transforming into malignant tumor cells, the activity of the glycolysis pathway, oxidative phosphorylation pathway, angiogenesis pathway, DNA repair pathway, mTORC1 signaling pathway gradually increased over time. However, P53 pathway, apoptosis signaling pathway activity then steadily decreased (Fig S2f). Similarly, we performed GSVA analysis on malignant and nonmalignant cells from the three groups. We found that the glycolysis pathway, oxidative phosphorylation pathway, MYC-targets, E2F-targets, DNA repair pathway, and mTORC1 signaling pathway were significantly enriched in MalignantNCT cells derived from the NCT group (Fig. 3g). The metabolic reprogramming enables cancer cells to resist anti-cancer drugs, thereby developing chemoresistance (24). To find the hub genes that cause the malignant transformation of epithelial cells, through Single-Cell Regulatory Network Inference and Clustering (SCENIC) analysis, we found that E2F1, BRCA1, PURA, NKX2-1, NFIC, ETV7, STAT1, EGR1, and CEBPD were highly expressed in malignant cells (cluster 2, 6, 11) from the Control group. In contrast, the malignant cells from the NCT group (clusters 1, 7, 8, 9) have high expression of transcription factors (TFs) such as PATZ1, SIX5, BATF, IRF1, FOXA1, and CEBPG. After neoadjuvant chemotherapy, the increased expression of these TFs promoted the occurrence of lung adenocarcinoma complex phenotypic remodeling (Fig. 3h).

Tumor cells have significant heterogeneity. We re-clustered the malignant cells and obtained 13 sub-clusters (Fig. 3i). Cluster 1, 2, 5, 6, 8, and 10 were derived from the NCT group (Fig. 3i). Through the analysis of the metabolism of these cell subclusters, we found that clusters 5 (marker genes: PCP4/NPW/VSIG1), 6 (marker genes: ERG1/HSPA6), and 10 (marker genes: C9orf172/SLC39A10) from the NCT group showed high levels of glycolysis, oxidative phosphorylation and pyruvate

203 metabolism (Fig. 3k). GSVA analysis also showed that the glycolysis and oxidative
204 phosphorylation signaling pathway-related genes were significantly enriched in
205 clusters 5, 6, and 10 (Fig. 3l). Similarly, we re-clustered nonmalignant cells to obtain
206 16 sub-clusters, of which clusters 1, 3, 8, 11, 12，13，15 were from the NCT group,
207 and the rest were from the Control group (Fig S2g, h). Clusters 4 and 7 from the
208 Control group showed high levels of glycolysis and oxidative phosphorylation (Fig
209 S2i, j), which was the opposite of the glucose metabolism of malignant cells from the
210 Control group.
211
212 **Changes in stroma cells resulted from neoadjuvant chemotherapy.**
213 To investigate stromal cell dynamics in the tumor microenvironment (TME), we
214 obtained 8944 presumed stromal cells, as shown in Fig. 1c. We re-clustered them into
215 five sub-populations, including COL14A1-positive fibroblasts, endothelial-1,
216 endothelial-2, myofibroblasts, pericytes, and smooth muscle cells (SMC) (Fig. 4a-c)
217 (25-27). Detailed expression of the marker genes in each cell type is outlined in Fig.
218 4c. Herein, we noticed a significant difference between the distribution of each of
219 these five clusters in patients receiving varied types of treatment. The COL14A1-
220 positive fibroblasts comprised the main fibroblast types in NCT groups, in which both
221 endothelial 1 & 2 were mainly found. Pericyte and SMC were presented in all three
222 groups. In contrast, myofibroblasts exclusively originated from the control group.
223 According to previous research, myofibroblast has been described as a cancer-
224 associated fibroblast that participated in extensive tissue remodeling, angiogenesis,
225 and tumor progression (25, 26). Therefore, this finding revealed that NCT and
226 immunotherapy significantly altered the stromal cell composition in the tumor
227 microenvironment.
228 To explore the activity of known biological pathways in these stromal cells, we
229 performed functional enrichment analysis. In particular, GSVA analysis exhibited that
230 endothelial 1 & 2 shared several up-regulated pathways related to cell proliferation
231 and fate regulation, including IL6-JAK-STAT3, TGFβ, and WNT-β catenin signaling.

232 Besides, pathways associated with energy metabolisms such as glycolysis and
233 hypoxia were up-regulated in myofibroblast, whereas pericyte was characterized by
234 enriched oxidative phosphorylation and adipogenesis (Fig. 4d). Meanwhile, when
235 comparing the GSVA scores of these biological processes between patients from
236 control or NCT groups, we noted that the stromal cells exhibited enhanced metabolic
237 levels after NCT, as represented by up-regulated glycolysis, oxidative
238 phosphorylation, and fatty acid metabolism pathways (Fig. 4e).

239 Considering the essential fibroblasts and their complicated function in shaping
240 the tumor microenvironment, we further re-clustered them into ten subgroups (Fig. 4f-
241 h). As shown in Fig. 4i-j, the GSVA score of the metabolic pathways, including
242 glycolysis and oxidative phosphorylation, and pyruvate metabolism and citrate cycle
243 (TCA cycle), were up-regulated in clusters 5, 6, and 9. Intriguingly, the upregulation
244 of these pathways was mainly observed in NCT groups (Fig S3a). The three clusters
245 were represented by distinct gene expression profiles, such as overexpressed MYH11
246 in cluster 5, RGS5 in cluster 6, and TOP2A in cluster 9. Since the potential
247 involvement of these genes in the manipulation of fibroblast metabolism has never
248 been proposed yet, they might serve as new specific markers of the fibroblast subtype
249 with such a high metabolic rate in the tumor microenvironment. Besides, the SCENIC
250 analysis demonstrated that MEF2C, NFIA, and RAD21 might drive the formation of
251 these clusters, respectively (Fig S3c). Further in vitro studies were required to
252 elucidate these notable fibroblasts' potential function and driver genes in LUAD's
253 development and response to NCT. Conclusively, cellular dynamics in stromal cells
254 support a consistent phenotypic shift of fibroblasts towards an increased metabolic
255 level after preoperative chemotherapy.

256

257 **Chemotherapy drove tumor-associated macrophages to turn more into**
258 **phenotypes that promote tumor progression.**

259 In the process of cancer formation, tumor-associated macrophages (Tumor-
260 Associated Macrophages, TAM) have an essential influence on the inflammatory

261 response in the tumor microenvironment (28). To study the effects of chemotherapy
262 on TAMs, we first extracted all macrophages (10526 cells) and re-clustered them into
263 ten cell clusters (Fig. 5a). From Fig. 1e, we can see that the proportion of
264 macrophages after chemotherapy was reduced.

265 The cell clusters derived from the Control group were 1/2/3/5/7 clusters, those
266 from the NCT group were mainly 0/4/8 clusters, and the number of cells in the 6/9
267 clusters from the Control group and the NCT group was similar (Fig. 5a). The
268 proportion of cells in cluster 0 (marker genes: CXCL8/ CCL20/CHIT1), 4 (marker
269 genes: CCL3/ CCL4/ SEPP1), 8 (marker genes: ARG2/ S100A2) decreased after
270 chemotherapy, while the remaining cell clusters increased (Fig. 5b, c). Through the
271 GSVA analysis, we found that glycolysis, angiogenesis, PI3K-AKT-mTOR-signaling,
272 IL6-JAK-STAT3-signaling, hypoxia, TGF-beta-signaling, and other signaling
273 pathways were significantly enriched in cluster 0/1/8. Promoting inflammation-related
274 signaling pathways such as TNF-signaling-via-NFKB, inflammatory-response, Notch-
275 signaling, fatty-acid-metabolism, and oxidative-phosphorylation were increased
276 dramatically in clusters 2/4/7/9 (Fig. 5d).

277 Similarly, we found that glycolysis/gluconeogenesis, amino sugar and nucleotide
278 sugar metabolism, alanine, aspartate, and glutamate metabolism were more active in
279 the 0/1/8 cluster. In contrast, oxidative phosphorylation, citrate cycle, pyruvate
280 metabolism, fatty acid elongation, fatty acid biosynthesis, etc., were more active in
281 clusters 2/4/7/9 (Fig. 5e). According to the GSVA analysis, the
282 glycolysis/gluconeogenesis signaling pathway was significantly enriched in
283 macrophages from the NCT group. In contrast, macrophages from the Control group
284 showed a high activity in oxidative phosphorylation, fatty acid elongation, fatty acid
285 degradation, fatty acid biosynthesis, and citrate cycle (TCA cycle) (Fig. 5f). These
286 results indicate that significant metabolic reprogramming occurred in tumor-
287 associated macrophages after chemotherapy, and different TAMs cell clusters also
288 showed huge metabolic differences. In general, our results revealed that
289 chemotherapy could promote glycolysis of TAMs and inhibit fatty acid metabolism.

To explore the key genes that regulate the differences in the metabolism of each subcluster of macrophages, we performed a SCENIC analysis. We found that HES, PPARG, SPI1, CEBPB, and IRF7 were highly expressed in cluster 0/1, which may be the key genes that regulate the conversion of macrophages into M2-like TAMs, while clusters 2/4/7/9 highly expressed STAT1, STAT2, NFKB1, JUN, and FOS that regulate the conversion of macrophages to M1-like TAMs (Fig. 5g).

According to the gene expression of macrophages, we divided these 10 clusters of cells into three subtypes of macrophages through cluster analysis (Fig. 5h). We scored the expression levels of pro-inflammatory and anti-inflammatory genes in all macrophages. We displayed each color-coded macrophage subtype's M1 and M2 scores (left) and pro-inflammatory and anti-inflammatory scores (right) through a scatter plot.

Similarly, we found that 0/1/8 cluster cells exhibited M2-like polarization and anti-inflammatory properties, while 2/4/7/9 exhibited M1-like polarization and pro-inflammatory properties (Fig. 5i). Based on these analyses, we divided these 10 clusters of macrophage subtypes into three categories: M1-like polarized phenotype was defined as Anti-mac; M2-like polarized phenotype was defined as Pro-mac; those without obvious polarized phenotype were defined as Mix (Fig. 5j). We found that the proportion of Pro-mac in the tumor microenvironment increased after chemotherapy, especially in the case of NCT-1 (Fig. 5k). Interestingly, we found that two subtypes, Anti-mac and Mix, can be converted to Pro-mac through pseudotime time analysis. In this evolution process, the high expression of LYZ, FBP1, ALOX5AP, MARCO, S100A9, FN1, CXCL8, APOC1CTSL, and other genes may have played an essential role in promoting the conversion of Anti-mac to Pro-mac. This suggests that we can change the phenotype of TAMs in the tumor microenvironment by altering the expression of these genes.

Chemo-driven Pro-mac and Anti-mac metabolic reprogramming exerted diametrically opposite effects on tumor cells.

To further verify the remodeling effect of chemotherapy on the functional phenotype of TAMs in the tumor microenvironment, we first used the FindAllMarkers function in the Seurat package to find the marker genes of Pro-mac, Anti-mac, and Mix cells. Pro-mac was mainly characterized by high expression of CXCL8, ARG1, CREM, CD206, STAT6, CCL22, MMP7, and CCL3L3, while Anti-mac was mainly characterized by high expression of CD86, HLA-DR, PLAC8, CXCL10, COX2, IL15R, and SCGB3A1 (Fig. 6a). Based on these marker genes, we sorted out Anti-mac cells (CD45+CD11b+CD86+) and Pro-mac cells (CD45+CD11b+ARG+) by flow cytometry (Fig. 6b). To verify whether the cells we sorted were the cell population we wanted, we re-verified the positive rates of Pro-mac and Anti-mac cells by flow cytometry (Fig. 6c). Our results showed that the proportion of Pro-mac cells in lung adenocarcinoma tissues after neoadjuvant chemotherapy increased significantly (Fig. 6d). In fact, by performing immunofluorescence staining on lung adenocarcinoma tissue samples derived from surgery alone and neoadjuvant chemotherapy, we also found that the proportion of cells marked by the marker gene CD206 of M2-like TAMs increased significantly after chemotherapy (Fig. 6e). Macrophages can promote tumor progression by secreting many cytokines. By analyzing the differentially expressed genes of Pro-mac and Anti-mac cells, we found IL10, PDCD1LG2, PDGF, VEGF, MMP9, CXCL9, CXCR4, IL22, KLF4, and TGF-β were highly expressed in Pro-mac cells that promote tumor growth, angiogenesis and suppress tumor immunity (Fig. 6f). We obtained the Pro-mac and Anti-mac cells from 12 cases (6 cases of surgery alone, 6 cases of surgical samples after neoadjuvant chemotherapy) by flow cytometry. We named them Control Anti-mac, Control Pro-mac, NCT Anti-mac, NCT Pro-mac. After placing them in a cell culture flask for 24 hours, the content of some key cytokines in the supernatant of the culture medium was detected by enzyme-linked immunosorbent assay (ELISA). The levels of MMP9, EGF, and VEGF secreted by Pro-mac after neoadjuvant chemotherapy were significantly higher than those of Pro-mac from the surgery alone group. MMP9, EGF, VEGF, and IL10 secreted by Pro-mac were significantly higher than Anti-mac

348 (Fig. 6g). Similarly, when Control Anti-mac, Control Pro-mac, NCT Anti-mac, and
349 NCT Pro-mac were inoculated subcutaneously with A549 cells at a ratio of 1:1
350 (Reinjection of macrophages two weeks later), we also found that NCT Pro-mac can
351 significantly promote tumor growth. Interestingly, NCT Anti-mac in the tumor
352 microenvironment after chemotherapy can significantly inhibit the growth of tumor
353 cells, and this inhibitory ability was stronger than Control Anti-mac (Fig. 6h, i).
354 Our previous analysis found that Pro-mac glycolysis-related signaling pathways
355 were significantly enriched, while in Anti-mac, oxidative phosphorylation and fatty
356 acid metabolism signaling pathways were greatly enhanced (Fig. 6j). In vitro
357 experiments show that NCT Pro-mac's ability to take up glucose and produce lactate
358 was considerably more potent than other cells (Fig. 6k). It was worth noting that the
359 glycolysis level of NCT Anti-mac was markedly higher than that of Control Anti-mac
360 (Fig. 6l). When we placed the Pro-mac and Anti-mac in a 24-well plate and co-
361 cultured with A549 cells in the Transwell chamber, we found that NCT Pro-mac can
362 significantly enhance the invasion ability of A549 cells. At the same time, NCT Anti-
363 mac showed a stronger ability to inhibit tumor invasion than Control Anti-mac (Fig.
364 6m). However, when we used 2-DG (800uM, the concentration determined in pre-
365 experiment) to inhibit the glycolysis of TAMs, the ability of Pro-mac to promote
366 tumor progression was significantly weakened, and the power of NCT Anti-mac to
367 suppress tumors was also considerably reduced (Fig. 6m). By mixing these cells with
368 macrophages for 3D culture, we found that the ability of NCT Anti-mac to inhibit
369 tumor proliferation was significantly weakened when inhibiting its glycolytic activity.
370 This showed that glycolysis could enhance the ability of Pro-mac to promote tumor
371 progression and increase the capacity of Anti-mac to inhibit tumors (Fig. 6n). Finally,
372 through in vivo experiments, we inoculated a mixture of TAMs and A549 to nude
373 mice and obtained the same experimental results as in Fig. 6m/n (Fig. 6o).
374
375 **Chemotherapy treatment-induced remodeling of T and B cells.**
376 Considering the essential role of the tumor microenvironment, especially the

377 immune infiltration level, in tumor development and response to therapy, we next
378 investigated the characteristics of T and B cells. In our study, 22530 T cells were
379 detected, which accounted for 26.9% of the total. We noticed that the re-clustered T
380 cells could not be visibly distinguished among patients receiving different therapeutic
381 regimens (Fig S6a-b). According to the expression of a series of canonical markers of
382 T cell subtypes, the T cells were divided into CD4+ T (marked by LTB, CD45RO,
383 etc.), CD8+ T (marked by NKG7, GZMA, GZMB, CD8A, etc.), and Tregs (marked
384 by FOXP3, CTLA4, etc.) (12, 21, 29) (Fig S6c-d). The detailed expression profile of
385 these marker genes is exhibited in Fig S6e. Meanwhile, aside from these previously
386 published T-cell markers, we also noted the specific upregulation of several genes in a
387 particular cluster. At the same time, their expression specificity has not been
388 elucidated yet.

389 As the major executor of tumor immunology, CD8+ T cells are thought to
390 differentiate into cytotoxic T cells (CTLs) and specifically recognize endogenous
391 antigenic peptides presented by the major histocompatibility complex I, thereby
392 eliminating tumor cells (30). By comparing the composition of T cell subtypes in
393 LUAD cells derived from different groups, we found that the proportion of CD8+T
394 cells in the NCT group was significantly higher than those in patients receiving only
395 surgical treatment (Fig S6d). Therefore, we focused on CD8+ T cells for subsequent
396 analyses and re-clustered them into five new subgroups, in which clusters 1-4 were
397 mainly derived from the NCT group. In contrast, cluster 5 was predominantly
398 enriched in the control group (Fig S6f-k).

399 We next explored the expression profile of genes associated with T cell's function
400 in each CD8+ T sub-cluster. As depicted in Fig S6i, clusters 1 and 2 were
401 characterized by up-regulated naïve T cell markers, such as TCF7, LEF1, and CCR7,
402 whereas genes associated with immune inhibition, like TIGIT, CTLA4, PDCD1, and
403 HAVCR2, were enriched explicitly in cluster 3. Cytotoxic function-related genes,
404 including GZMA GNLY, PRF1, GZMP, and GZMK, IFNG, IL2, were respectively
405 overexpressed in clusters 4 and 5. Based on this evidence, we defined clusters 1 and 2

406 as naive T, three as regulatory/exhausted T, and 4 & 5 as cytotoxic T cells.
407 Intriguingly, regarding both the sample origins and expression profiles of CD8+ T
408 cells in clusters 4 and 5, we can reasonably hypothesize that NCT treatment
409 potentially induces the reprogramming of CD8+ cytotoxic cells. To further verify this
410 statement, we performed pseudotime-ordered trajectory analysis to monitor the
411 dynamic view of CD8+ T cells' reprogramming process via Monocle. As shown in
412 Fig S6l-p, three phases were detected in these clusters. Cluster 1, which exhibited the
413 lowest cytotoxicity, was designated as the "root" state according to pseudotime.

414 In contrast, the immune inhibition-related genes like LAG3, TIGIT, and PDCD1,
415 and cytotoxicity-related genes such as GZMB and IFNG were respectively activated
416 in phases 2 and 3. This phenomenon is consistent with our T cell phenotype
417 classification mentioned above. Then, our results showed differentiation paths from
418 naive T to Treg/exhausted cells and cytotoxic cells. Considering the transcriptional
419 changes associated with T cell reprogramming, naive T cells (phase 1) expressing
420 high CCR6 and TCF7 differentiate into two distinct fates, clusters 4 and 5, in phase 3.
421 Notably, the cells positioned at the cluster 4 branch were characterized by higher
422 cytotoxicity than in cluster 5 (Fig S6l, m, o). Regarding the sample origins of the two
423 clusters, these findings demonstrated that NCT treatment ignites a relatively more
424 robust immune cytotoxic response towards tumor cells, which could be partly
425 explained by the excessive production of neoantigen caused by NCT-induced DNA
426 damage.

427 SCENIC analyses suggested that distinct transcriptional mechanisms drove the
428 differentiation of naive T cells to either cluster 4 or 5. As revealed in Supplementary
429 Fig. 6q, the cytotoxic cells derived from NCT-treated LUAD patients (cluster 4) were
430 characterized by increased activation of FOSL2-extended, REL, YBX1, and NF-KB
431 pathways. In contrast, those from the control group (cluster 5) had up-regulated JUN,
432 FOSB, and ELF3 extended pathways. Together, our results revealed that preoperative
433 chemotherapy prompts the naïve T cells to differentiate towards a more cytotoxic
434 phenotype.

435 As for B cells, only 3902 (4.6%) cells were detected. 475 cells were derived from
436 the control group, while 3427 were from the NCT group (Fig S4a). Herein, we re-
437 clustered the B cells into two sub-clusters. Based on canonical cell markers, class-
438 switched memory B-cells (marked by CD19, CD37, and HLA-DRA) and plasma cells
439 (marked by IGHA2, IGHG4, and CD38) were defined (Fig S4a-c). The former
440 compromised the majority of the total B cells (80.7%). Notably, the sample origins of
441 the B cells demonstrated that a higher proportion of plasma cells characterized the
442 control groups. In contrast, the class-switched memory B cells were significantly
443 enriched in preoperatively treated patients.
444 Meanwhile, we performed GSVA analysis to explore several key biological
445 pathways in the B cells derived from different groups. As depicted in Fig S4d, B cells
446 from the control group exhibited significant activating ways associated with
447 metabolism and energy supply, including glycolysis and oxidative phosphorylation.
448 However, the B cells derived from the NCT group exerted essential roles in most of
449 the pathways, including glycolysis, fatty acid metabolism, apoptosis, and hypoxia.
450 Overall, our observations demonstrated that NCT not only induced T cell
451 reprogramming but also extensively impacted the composition and function of B cells
452 in the tumor microenvironment.
453
454 **Crosstalk among tumor and immune cells**
455 The tumor microenvironment consists of numerous cell types, and the importance
456 of crosstalk between cancer and immune cells has been implicated in various
457 biological processes associated with tumor development (21, 29, 31). As depicted in
458 Fig S7a-b and Fig S5a, the interactions between malignant and macrophages exhibited
459 the strongest activity in both control and NCT groups, highlighting the important role
460 of the macrophage in tumor immunology. Notably, we noted that the cell-to-cell
461 communications among different cell types, especially between tumoral and immune
462 cells such as cytotoxic CD8+ T, Treg, and memory B, were significantly strengthened
463 in the NCT group. Specifically, we further investigated the ligand-receptor atlas

464 within and between tumor cells and immune cells, which seemed to be quite reshaped
465 by NCT (Fig S7c-d, Fig S5b). For example, MIF-CXCR4, whose activation usually
466 promotes leukocyte recruitment (32), was increasingly activated in the NCT group
467 between malignant and memory B, CD4+ T, and cytotoxic CD8+ T, whereas inhibited
468 in macrophages. Meanwhile, MDK-NCL exhibited a similar activating phenotype
469 with MIF-CXCR4, but its function in shaping the tumor microenvironment has never
470 been reported. So, it might serve as a potential target of immune checkpoint inhibitor
471 treatment in the future.

472 Given the above-mentioned NCT-induced immune activation, which was
473 characterized by CD8+ T with higher cytotoxicity and an increased proportion of
474 class-switched memory B cells, these findings further clarified that NCT could ignite
475 a strong intrinsic immune response towards tumor cells. However, the inhibitory
476 interaction pairs LGALS9-CD44 and LGALS9-HAVCR2 was abnormally activated in
477 the NCT group between malignant and several T cells or macrophages (33). Its exact
478 role in such conditions still requires further exploration.

479 In summary, our study revealed that the LUAD tissues that have experienced
480 NCT had a distinct landscape of intracellular interactions, which might provide new
481 ideas for future research focusing on implementing immunotherapy in the
482 comprehensive anti-tumor therapeutic regimen.

483

484 Discussion

485 Although important advances in chemotherapy have reduced the mortality of
486 cancer patients, the 5-year survival rate is still gloomy, mainly due to the inherent or
487 acquired mechanism of anti-tumor drug resistance (34). Chemoresistance results
488 from complex reprogramming processes, such as drug export/import, drug
489 detoxification, DNA damage repair, and cell apoptosis. Recently, the correlation
490 between metabolic regulation and chemoresistance has received great attention. More
491 and more efforts are devoted to targeted metabolism to overcome chemoresistance
492 (35). The classic mechanism is to target the transport of anti-cancer drugs by

493 increasing the activity of the efflux pump, such as the adenosine triphosphate (ATP)
494 binding cassette (ABC) transporter. Cancer cells exhibit a special metabolic
495 phenotype-aerobic glycolysis, quickly transporting and consuming glucose to produce
496 ATP and promote drug efflux. PI3K/AKT pathway is activated by producing 3'-
497 phosphorylated phosphoinositol, which is an important signaling pathway for lung
498 cancer MDR (36). Glycolysis is beneficial to cancer cells by producing ATP faster,
499 providing many intermediates for violent biosynthesis, maintaining redox balance,
500 and creating a microenvironment with low immunity (24). The combination therapy
501 of shikonin+2-DG could inhibit glycolytic phenotype, migration, and invasion by
502 regulating the Akt/HIF1α/HK-2 signal axis (37).

503 Normal and healthy cells mainly produce energy through OXPHOS. However,
504 due to rapid cell growth and frequent division, cancer cells face impressive metabolic
505 challenges, which force them to adjust their energy metabolism to meet these needs
506 (38). It is generally believed that cancer cells mainly obtain energy through
507 glycolysis, which is named the Warburg effect. After chemotherapy, cancer cells
508 change their metabolism from glycolysis to OXPHOS. This process is regulated by
509 the SIRT1-PGC1α signaling pathway, thus increasing the resistance of cells to
510 chemotherapy (39). Drug-resistant cancer cells can often be re-sensitized to anti-
511 cancer treatments by targeting the metabolic pathways of import, catabolism, and
512 synthesis of basic cell components (40). Recent studies have determined the cancer-
513 promoting function of mitochondrial oxidative phosphorylation (OXPHOS) by
514 regulating cell growth and redox homeostasis (41). Our study also found that after
515 chemotherapy, the glycolysis and oxidative phosphorylation of tumor cells was
516 enhanced. This metabolic reprogramming may enable cancer cells to have higher
517 proliferation, invasion, and metastasis capabilities.

518 Tumor endothelial cells (ECs) have high glycolytic metabolism, shunting
519 intermediates to nucleotide synthesis. Blocking of the glycolysis activator PFKFB3 in
520 EC cells does not affect tumor growth. Still, it reduces cancer cell invasion,
521 intravascular, and metastasis by normalizing tumor blood vessels, thereby improving

522 blood vessel maturation and perfusion. PFKFB3 inhibition tightens the vascular
523 barrier by reducing VE-cadherin endocytosis in endothelial cells and reduces
524 glycolysis to make cells more quiescent and adherent (by up-regulating N-cadherin);
525 it also reduces NF-κB signaling to reduce the expression of cancer cell adhesion
526 molecules in ECs. PFKFB3 blockade therapy also improves chemotherapy for
527 primary and metastatic tumors (42).

528 Due to rapid cell growth and frequent division in tumor cells, cancer cells face
529 impressive metabolic challenges, which force them to adjust energy metabolism to
530 meet these needs, namely metabolic reprogramming (43). However, studies have
531 shown that metabolic plasticity in tumors is contributed by the glycolytic phenotype
532 (as explained by Warburg) and that mitochondrial energy reprogramming has recently
533 been identified as a feature of tumors (44). Chemotherapy can increase
534 SIRT1/PGC1α-dependent oxidative phosphorylation (OXPHOS) in tumor cells,
535 thereby promoting the survival of colorectal tumors during treatment. This
536 phenomenon was also observed in chemotherapy-exposed liver metastases, which
537 strongly suggests that chemotherapy causes long-term changes in tumor metabolism,
538 which may interfere with drug efficacy (39). In addition, elevated glycolysis and
539 OXPHOS promote epithelial-mesenchymal transition and cancer stem cell (CSC)
540 phenotype in tumor cells (45). Therefore, recent research emphasizes the mixed
541 glycolysis/OXPHOS phenotype rather than the phenotype that relies excessively on
542 glycolysis to meet cellular energy requirements, thereby significantly promoting
543 aggressiveness and treatment resistance (44). Chemotherapy has a significant effect
544 on the metabolic reprogramming of tumor cells and profoundly affects stromal and
545 immune cells' metabolism in the tumor microenvironment.

546 Theoretically, chemical drugs can inhibit tumorigenesis by blocking the
547 proliferation of tumor cells or depositing in tumor cell apoptosis, but this
548 unintentionally causes "tissue damage." The body will mistake this tumor-specific
549 damage for normal tissue damage and then inevitably activate the tissue damage
550 repair mechanism dominated by TAM (46). The result of this effect is that tumors will

grow rapidly, and patients will develop resistance to anti-tumor chemotherapy.

Meanwhile, as suggested by Parra et al., neoadjuvant chemotherapy exerted PD-L1 upregulation in NSCLC patients. It increased the density of CD68+ macrophages, which were associated with better outcomes in both univariate and multivariate analyses (47). However, opposite results were also reported by Talebian et al. that NSCLC patients treated with radiotherapy, rather than a platinum-based standard-of-care chemotherapy, displayed a decrease in lymphoid cells and a relative increase in macrophages (48). Therefore, the role of TAMs in LUAD cells' response to chemotherapy still requires further investigation.

In conclusion, our research reveals the remodeling effect of chemotherapy on tumor microenvironment. However, this study still has many limitations. Firstly, only 9 samples were included in our study, and the number of samples is a defect of our study. Secondly, our study did not detect other causes of tumor heterogeneity, such as EGFR-mutant or ALK-translocated. We explored the possible impact of these factors and found that there was no significant difference in the expression of EGFR and other genes between the NCT group and the Control group (Table S1). Thirdly, our data can only reflect the change in gene expression of various types of cells in the tumor microenvironment after chemotherapy. We can not draw a direct conclusion on whether chemotherapy will benefit patients or not. These need further study in the future.

Methods

Patients

All patients included in this study understood and signed written informed consent. The clinical samples of scRNA-seq came from patients diagnosed with LUAD, of which 4 cases received no treatment before surgery, and 5 cases received chemotherapy (Pemetrexed + Cisplatin). These samples were donated by inpatients in the Department of Thoracic Surgery, Zhongshan Hospital of Fudan University. After the lung adenocarcinoma tissue sample was taken, we first cut a small part to make

580 paraffin sections, and we dissociated the remaining tissue into a single-cell
581 suspension. $1x10^6$ cells were drawn from the single-cell suspension for single-cell
582 RNA sequencing.
583
584 **Preparation of single-cell suspensions**
585 For each patient, as described above, we dissociated the lung adenocarcinoma
586 tumor sample into a single-cell suspension and then took $1x10^6$ cells for single-cell
587 RNA sequencing. We used the Tumor Dissociation Kit (Miltenyi Biotec, Gladbach,
588 Germany) to digest tumor tissues with enzymes according to the manufacturer's
589 instructions. In short, we first cut the lung adenocarcinoma tissue sample into small
590 tissue pieces about $1cm^3$ with a surgical scalpel. We then transferred these small tissue
591 pieces to the MACS C tube containing 4.7 mL DMEM serum-free medium, 200 μL
592 Enzyme H, 100 μL Enzyme R, and 25 μL Enzyme A. After the tissue was incubated
593 and digested in a constant temperature incubator 37°C for 1 hour, the tissue was
594 mechanically separated by the MACS™ instrument. Repeat the above steps twice.
595 After the tissue sample was dissociated, the sample was filtered with a 40 μm filter to
596 remove the remaining large particles from the single-cell suspension. Centrifuge the
597 suspension at 300 × g for 7 minutes, and discard the supernatant.
598 Next, we used red blood cell lysate (10×) (Sigma-Aldrich, St. Louis, MO, USA)
599 to remove red blood cells from the single-cell suspension. In short, add 1x Lysis
600 Buffer to the centrifuge tube containing the single-cell pellet described above. The
601 cell suspension was then incubated at room temperature for 15 minutes. To improve
602 the quality of our samples, we also used a dead cell removal kit (Miltenyi Biotec) to
603 ensure that the cell survival rate of our sequencing samples was> 90%.
604
605 **The 10x scRNA-seq data analysis**
606 The R version used in our scRNA-seq data analysis study is 3.6.1. The cell
607 quality control criteria are as follows: 1) The number of expressed genes is less than
608 300 or greater than 5000; 2) 10% or more of UMI is localized to mitochondrial or
609 ribosomal genes. If they meet one of the criteria, the cells are excluded. After quality
610 standardization, we applied the Seurat R package (10) to analyze the scRNA-seq
611 data. First, we convert the scRNA-seq data into Seurat identifiable objects, and then

612 we use the "FindVariableFeatures" function to find the first 2000 highly variable
613 genes. After that, we applied principal component analysis (PCA) to reduce the
614 dimensionality of scRNA-seq data. The "RunTSNE" function is used to perform t-
615 distributed random neighborhood embedding (TSNE) to visualize various types of
616 cells. The "FindClusters" and "FindAllMarkers" functions are used for cluster analysis
617 of cell subclusters and detection of marker genes of cell subclusters.
618 Finally, according to the SingleR package (11), the CellMarker (http://bio-
619 bigdata.hrbmu.edu.cn/CellMarker/) data set, and the previous report (12), we
620 annotated different cell types. Simultaneously, some new potential marker genes were
621 verified through experiments.
622
623 **Analysis of Sub-Clusters of Cells in LUAD**
624 After preliminary classification and annotation of all cells, the annotated
625 epithelial cells, stromal cells, and immune cells are extracted through the
626 "SubsetData" function. Then, we apply the "FindClusters" and "FindAllMarkers"
627 functions to find the marker genes of each cell and perform dimensionality reduction
628 clustering on each extracted cell through TSNE. The sub-clusters are annotated by
629 dominantly expressed cell markers published by previous researchers. To select the
630 marker genes that meet the requirements, we set the following cut-off thresholds to
631 reveal the marker genes of each cluster: adjusted P-value <0.01 and multiple
632 changes>0.5.
633
634 **Estimation of the copy number variations**
635 To estimate the initial copy number variation (CNV) of each region, the R
636 package "scCancer" (13) was applied. The expression level of each cell was used as
637 the original input file for calculating CNV. Immune cells served as a background
638 reference for calculating the CNVs scores of other cells. In addition, the R package
639 "inferCNV" was used to quantify CNV in tumor cells as described previously (14).
640

641 **Definition of cell scores and signature**

642 To evaluate the M1/M2 polarization state and pro-/anti-inflammatory potential of
643 macrophages, we performed a GSVA analysis. We retrieved gene sets related to the
644 above functions from previous studies (15) and used them as references in this
645 analysis.

646 We used the average expression of a published list of characteristic genes for T
647 cell toxicity and exhaustion to define T cells' cytotoxicity, exhaustion, and
648 costimulation scores.

649

650 **Identification of gene markers of malignant cells**

651 We used the identified malignant cell marker genes in tumor cells to identify gene
652 expression characteristics in malignant cells. Then, we performed unsupervised NMF
653 to reveal the malignant characteristics of tumor cells through the NMF R package
654 (16).

655

656 **Trajectory analysis**

657 We used the monocle2 R package to analyze the trajectory of all cells to explore
658 the evolution of various types of cells in a single cell (17). First, apply the function
659 "newCellDataSet" to construct a data object that the monocle 2 R package can
660 recognize. Afterward, the differentially expressed genes identified by the Seurat R
661 package were selected for cell trajectory analysis. The "reduceDimension" function
662 was used to reduce the dimensionality. We used the "orderCells" function to project
663 cells on a pseudo-time trajectory to show the trend of cell evolution. A state consisting
664 of cells mainly derived from nonmalignant tissues in a cluster identified as epithelial
665 cells was defined as "root cells."

666

667 **Analyses of metabolic pathways**

668 To evaluate the activity of various metabolic pathways of each cell type, we
669 applied the algorithm developed by Xiao et al. (18). In short, the analysis of

metabolic programs is based on the average expression level of metabolic genes across cell types to indirectly reflect the metabolic activity of cells.

A variety of environmental factors potentially affect the metabolic reprogramming of tumors, such as chemotherapy, nutrient supply, and the environment where the cells are located. Therefore, exploring these factors and the cross-conversion between glycolysis and mitochondrial activity in various cells in the tumor microenvironment is essential for understanding the metabolic reprogramming of tumors.

We calculated the average gene expression levels in glycolysis and OXPHOS as indicators of glucose supply and mitochondrial activity, respectively. The data of genes that were responsive to the two groups of genes (known to be responsive to glycolysis and OXPHOS) used in the calculations were retrieved from the MsigDB database. At the same time, the cells were sorted by flow cytometry, and the contents of various metabolites were tested, in turn, to verify whether they were consistent with gene expression levels.

Cell Interaction Network analysis

To study the cell-to-cell interactions between tumors and nonmalignant cells, immune cells, and stromal cells, we applied the R package "CellChat" (19) and "CellPhoneDB" Python package for analysis (20). The crosstalk analysis between cells through the "CellChat" package was as follows: (1) First, use the "createCellChat" function to create a data set object that can be identified by "CellChat"; (2) Then use "aggregateNet", "computeCommunProbPathway", and "computeCommunProb" function to automatically infer the possible cellular communication network between cells; (3) Finally, the "netVisual_aggregate", "netVisual_bubble" and "netVisual_signalingRole" functions were used to visualize the interaction between these cells. Then use the built-in parameters to apply the "CellPhoneDB" R package.

699 **Immunohistochemistry and immunofluorescence**

700 The paraffin-embedded lung cancer tissue sections were deparaffinized with
701 xylene and rehydrated. After antigen retrieval and removing endogenous peroxidase
702 activity in the tissue, an appropriate amount of goat serum was added dropwise to
703 block it for 30 minutes. Discard the blocking solution, add the primary antibody, and
704 incubate overnight at 4 degrees. After removing the primary antibody and washing
705 thoroughly, add the secondary antibody to incubate for 1 hour, and then add DAB
706 chromogenic reagent (Gene Tech, China) for color development. Finally, hematoxylin
707 is used for nuclear dyeing.

708 As mentioned in the above immunohistochemistry experiment, the steps before
709 incubating the primary antibody are the same. Incubate with the corresponding
710 primary and secondary antibodies with green and red fluorescent dyes, respectively,
711 and then use DAPI to stain the nuclei.

712

713 **Flow cytometry assay**

714 Cells and APC-conjugated mouse anti-human CD45, FITC-conjugated mouse
715 anti-human CD11b, BV421-conjugated mouse anti-human ARG1, as well as pe-cy-
716 conjugated mouse anti-human CD86 (5 μL/10^6 cells; BD Biosciences) were incubated
717 on ice for 30 minutes. Then, FACSAria III (BD Biosciences) was used to quantify the
718 required cells, and FlowJo software (TreeStar, Woodburn, OR, USA) was used to
719 analyze the results.

720

721 **Animal experiments**

722 All animals involved in this study were treated humanely and received standard
723 care. The animal experimental procedures were approved by the Institutional Review
724 Board of Zhongshan Hospital of Fudan University (Shanghai, China). In this
725 experiment, we housed male athymic nude mice (BALB/cASlac-nu) in a specific
726 pathogen-free environment. We mixed treated A549 cells and TAMs to make a 1:1
727 cell mixture at a cell concentration of $5x10^6$ cells/ml. Take 0.05ml of the mixed

suspension of cells and Matrigel, and implant them into the lung thoracic cavity of nude mice for in situ tumor formation experiments.

Animals were sacrificed when one of the following signs of disease was observed: tumor ulceration (greater than 0.5 cm); inability to move or eat; or serious injury. Changes in tumor size were detected using an optical imaging system for in vivo small animals (IVIS Spectrum, PerkinElmer, USA).

Statistical Analysis

The statistical tools, methods, and thresholds of each analysis are clearly described in the results or detailed in the legend or materials and methods.

Abbreviations

LUAD: lung adenocarcinoma
NCT: neoadjuvant chemotherapy
TME: tumor microenvironment
TSNE: t-distributed random neighborhood embedding
CNV: copy number variation
SCENIC: Single-Cell Regulatory Network Inference and Clustering
SMC: smooth muscle cells
TCA cycle: pyruvate metabolism and citrate cycle
TAM: Tumor-Associated Macrophages
CTLs: cytotoxic T cells
OXPHOS: oxidative phosphorylation
CSC: cancer stem cell

Declarations:

Ethics approval and consent to participate

A total of 9 patients were included in this study. The Ethics Committee of Zhongshan Hospital of Fudan University approved our research (B2021-230R), and the content of the study complies with the Helsinki Declaration.

A total of 60 animals were involved in this study. They were treated humanely and

received standard care. The animal experimental procedures were approved by the Institutional Review Board of Zhongshan Hospital of Fudan University (Y2021-137) (Shanghai, China).

Availability of data and material

The single-cell sequencing data used in this study and other experimental data can be obtained from the figshare (10.6084/m9.figshare.24797265).

Acknowledgment

We thank OE Biotechnology Co., Ltd. (Shanghai, China) for helping us perform single-cell sequencing analysis of lung adenocarcinoma surgical samples. We thank International Science Editing Co. for providing language editing services for our papers.

Author contributions

S.Y.Y, Y.W.H., G.S.B, C.Z., and W.J. designed the research; Y.W.H., L.C., J.Q.L., T.L., M.N.Z., G.S.B., M.L., J.Q.L., Z.Y.H., Y.S.Z., J.J.X, C.Z., Z.W.L., W.J., Q.W., and L.J.T. performed the research; Y.W.H., C.Z., L.X., G.J.W., and G.S.B. analyzed the data; Y.W.H., G.S.B., J.Q.L., L.X., and C.Z. wrote the paper. Final approval of the manuscript: All authors.

Competing interests

The authors have no conflicts of interest to declare.

Consent for publication

All of the authors have consented to publication.

Funding

This research was funded by the Yangfan plan program of Shanghai (No. 22YF107300), the National Natural Science Foundation of China (No. 82203645), the China Postdoctoral Science Foundation (No. 2023M730655), the Natural Science Foundation of Shanghai, China (No. 22ZR1411900), and the Special Foundation for Supporting Biomedical Technology of Shanghai, China (No. 22S11900300).

References

1. Siegel RL, Miller KD, Jemal A. Cancer statistics, 2020. CA Cancer J Clin 2020; 70(1): 7-30. https://doi.org/10.3322/caac.21590.

2. Ren L, Zhong X, Liu W, Xu D, Lei Y, Zhou J, et al. Clinical significance of a circulating tumor cell-based classifier in stage ib lung adenocarcinoma: a multicenter, cohort study. Ann Surg 2023. https://doi.org/10.1097/SLA.0000000000004780.

3. Ekoh OC, Okoro U, Ugwu D, Ali R, Okafor S, Ugwuja D, et al. Novel dipeptides bearing sulfonamide as antimalarial and antitrypanosomal agents: synthesis and molecular docking. Med Chem 2022. https://doi.org/10.2174/1573406417666210604101201.

4. Cai X, Hu B, Liu S, Liu M, Huang Y, Lei P, et al. Overexpression of close homolog of l1 enhances the chemosensitivity of lung cancer cells via inhibition of the akt pathway. Oncol Lett 2020; 20(4): 111. https://doi.org/10.3892/ol.2020.11972.

5. Bondarenko M, Le Grand M, Shaked Y, Raviv Z, Chapuisat G, Carrère C, et al. Metronomic chemotherapy modulates clonal interactions to prevent drug resistance in non-small cell lung cancer. Cancers (Basel) 2021; 13(9). https://doi.org/10.3390/cancers13092239.

6. Katsumata S, Aokage K, Miyoshi T, Tane K, Nakamura H, Sugano M, et al. Differences of tumor microenvironment between stage i lepidic-positive and lepidic-negative lung adenocarcinomas. J Thorac Cardiovasc Surg 2018; 156(4): 1679-88. https://doi.org/10.1016/j.jtcvs.2018.05.053.

7. Ho PC, Bihuniak JD, Macintyre AN, Staron M, Liu X, Amezquita R, et al.

Phosphoenolpyruvate is a metabolic checkpoint of anti-tumor t cell responses. Cell 2015; 162(6): 1217-28. https://doi.org/10.1016/j.cell.2015.08.012.

8. Chang CH, Qiu J, O'Sullivan D, Buck MD, Noguchi T, Curtis JD, et al. Metabolic competition in the tumor microenvironment is a driver of cancer progression. Cell 2015; 162(6): 1229-41. https://doi.org/10.1016/j.cell.2015.08.016.

9. Reinfeld BI, Madden MZ, Wolf MM, Chytil A, Bader JE, Patterson AR, et al. Cell-programmed nutrient partitioning in the tumour microenvironment. Nature 2021; 593(7858): 282-8. https://doi.org/10.1038/s41586-021-03442-1.

10. Macosko EZ, Basu A, Satija R, Nemesh J, Shekhar K, Goldman M, et al. Highly parallel genome-wide expression profiling of individual cells using nanoliter droplets. Cell 2015; 161(5): 1202-14. https://doi.org/10.1016/j.cell.2015.05.002.

11. Aran D, Looney AP, Liu L, Wu E, Fong V, Hsu A, et al. Reference-based analysis of lung single-cell sequencing reveals a transitional profibrotic macrophage. Nat Immunol 2019; 20(2): 163-72. https://doi.org/10.1038/s41590-018-0276-y.

12. Lambrechts D, Wauters E, Boeckx B, Aibar S, Nittner D, Burton O, et al. Phenotype molding of stromal cells in the lung tumor microenvironment. Nat Med 2018; 24(8): 1277-89. https://doi.org/10.1038/s41591-018-0096-5.

13. Guo W, Wang D, Wang S, Shan Y, Liu C, Gu J. Sccancer: a package for automated processing of single-cell rna-seq data in cancer. Brief Bioinform 2021; 22(3). https://doi.org/10.1093/bib/bbaa127.

14. Müller S, Liu SJ, Di Lullo E, Malatesta M, Pollen AA, Nowakowski TJ, et al. Single-cell sequencing maps gene expression to mutational phylogenies in pdgf- and egf-driven gliomas. Mol Syst Biol 2016; 12(11): 889. https://doi.org/10.15252/msb.20166969.

15. Sun Y, Wu L, Zhong Y, Zhou K, Hou Y, Wang Z, et al. Single-cell landscape of the ecosystem in early-relapse hepatocellular carcinoma. Cell 2021; 184(2): 404-21. https://doi.org/10.1016/j.cell.2020.11.041.

16. Gaujoux R, Seoighe C. A flexible r package for nonnegative matrix factorization. Bmc Bioinformatics 2010; 11: 367. https://doi.org/10.1186/1471-2105-

11-367.

17. Qiu X, Mao Q, Tang Y, Wang L, Chawla R, Pliner HA, et al. Reversed graph embedding resolves complex single-cell trajectories. Nat Methods 2017; 14(10): 979-82. https://doi.org/10.1038/nmeth.4402.

18. Xiao Z, Dai Z, Locasale JW. Metabolic landscape of the tumor microenvironment at single cell resolution. Nat Commun 2019; 10(1): 3763. https://doi.org/10.1038/s41467-019-11738-0.

19. Jin S, Guerrero-Juarez CF, Zhang L, Chang I, Ramos R, Kuan CH, et al. Inference and analysis of cell-cell communication using cellchat. Nat Commun 2021; 12(1): 1088. https://doi.org/10.1038/s41467-021-21246-9.

20. Patel AP, Tirosh I, Trombetta JJ, Shalek AK, Gillespie SM, Wakimoto H, et al. Single-cell rna-seq highlights intratumoral heterogeneity in primary glioblastoma. Science 2014; 344(6190): 1396-401. https://doi.org/10.1126/science.1254257.

21. Chen Z, Huang Y, Hu Z, Zhao M, Li M, Bi G, et al. Landscape and dynamics of single tumor and immune cells in early and advanced-stage lung adenocarcinoma. Clin Transl Med 2021; 11(3): e350. https://doi.org/10.1002/ctm2.350.

22. Chen Z, Huang Y, Hu Z, Zhao M, Bian Y, Chen Z, et al. Dissecting the single-cell transcriptome network in patients with esophageal squamous cell carcinoma receiving operative paclitaxel plus platinum chemotherapy. Oncogenesis 2021; 10(10): 71. https://doi.org/10.1038/s41389-021-00359-2.

23. Faubert B, Solmonson A, Deberardinis RJ. Metabolic reprogramming and cancer progression. Science 2020; 368(6487). https://doi.org/10.1126/science.aaw5473.

24. Tuerhong A, Xu J, Shi S, Tan Z, Meng Q, Hua J, et al. Overcoming chemoresistance by targeting reprogrammed metabolism: the achilles' heel of pancreatic ductal adenocarcinoma. Cell Mol Life Sci 2021; 78(14): 5505-26. https://doi.org/10.1007/s00018-021-03866-y.

25. Kim N, Kim HK, Lee K, Hong Y, Cho JH, Choi JW, et al. Single-cell rna sequencing demonstrates the molecular and cellular reprogramming of metastatic

lung adenocarcinoma. Nat Commun 2020; 11(1): 2285. https://doi.org/10.1038/s41467-020-16164-1.

26. Xie T, Wang Y, Deng N, Huang G, Taghavifar F, Geng Y, et al. Single-cell deconvolution of fibroblast heterogeneity in mouse pulmonary fibrosis. Cell Rep 2018; 22(13): 3625-40. https://doi.org/10.1016/j.celrep.2018.03.010.

27. Vanlandewijck M, He L, Mäe MA, Andrae J, Ando K, Del GF, et al. A molecular atlas of cell types and zonation in the brain vasculature. Nature 2018; 554(7693): 475-80. https://doi.org/10.1038/nature25739.

28. Malfitano AM, Pisanti S, Napolitano F, Di Somma S, Martinelli R, Portella G. Tumor-associated macrophage status in cancer treatment. Cancers 2020; 12(7): 1987. https://doi.org/10.3390/cancers12071987.

29. Lu T, Yang X, Shi Y, Zhao M, Bi G, Liang J, et al. Single-cell transcriptome atlas of lung adenocarcinoma featured with ground glass nodules. Cell Discov 2020; 6: 69. https://doi.org/10.1038/s41421-020-00200-x.

30. Uzhachenko RV, Shanker A. Cd8(+) t lymphocyte and nk cell network: circuitry in the cytotoxic domain of immunity. Front Immunol 2019; 10: 1906. https://doi.org/10.3389/fimmu.2019.01906.

31. Raredon M, Adams TS, Suhail Y, Schupp JC, Poli S, Neumark N, et al. Single-cell connectomic analysis of adult mammalian lungs. Sci Adv 2019; 5(12): w3851. https://doi.org/10.1126/sciadv.aaw3851.

32. Bernhagen J, Krohn R, Lue H, Gregory JL, Zernecke A, Koenen RR, et al. Mif is a noncognate ligand of cxc chemokine receptors in inflammatory and atherogenic cell recruitment. Nat Med 2007; 13(5): 587-96. https://doi.org/10.1038/nm1567.

33. Anand P, Guillaumet-Adkins A, Dimitrova V, Yun H, Drier Y, Sotudeh N, et al. Single-cell rna-seq reveals developmental plasticity with coexisting oncogenic states and immune evasion programs in etp-all. Blood 2021; 137(18): 2463-80. https://doi.org/10.1182/blood.2019004547.

34. Sharma A. Chemoresistance in cancer cells: exosomes as potential regulators of therapeutic tumor heterogeneity. Nanomedicine (Lond) 2017; 12(17): 2137-48.

https://doi.org/10.2217/nnm-2017-0184.

35. Zhao Y, Butler EB, Tan M. Targeting cellular metabolism to improve cancer therapeutics. Cell Death Dis 2013; 4(3): e532. https://doi.org/10.1038/cddis.2013.60.

36. Harding JJ, Nandakumar S, Armenia J, Khalil DN, Albano M, Ly M, et al. Prospective genotyping of hepatocellular carcinoma: clinical implications of next-generation sequencing for matching patients to targeted and immune therapies. Clin Cancer Res 2019; 25(7): 2116-26. https://doi.org/10.1158/1078-0432.CCR-18-2293.

37. Gupta P, Jagavelu K, Mishra DP. Inhibition of nadph oxidase-4 potentiates 2-deoxy-d-glucose-induced suppression of glycolysis, migration, and invasion in glioblastoma cells: role of the akt/hif1α/hk-2 signaling axis. Antioxid Redox Signal 2015; 23(8): 665-81. https://doi.org/10.1089/ars.2014.5973.

38. Vander LC, Corbet C, Bastien E, Martherus R, Guilbaud C, Petit L, et al. Therapy-induced dna methylation inactivates mct1 and renders tumor cells vulnerable to mct4 inhibition. Cell Rep 2021; 35(9): 109202. https://doi.org/10.1016/j.celrep.2021.109202.

39. Vellinga TT, Borovski T, de Boer VC, Fatrai S, van Schelven S, Trumpi K, et al. Sirt1/pgc1α-dependent increase in oxidative phosphorylation supports chemotherapy resistance of colon cancer. Clin Cancer Res 2015; 21(12): 2870-9. https://doi.org/10.1158/1078-0432.CCR-14-2290.

40. Butler EB, Zhao Y, Muñoz-Pinedo C, Lu J, Tan M. Stalling the engine of resistance: targeting cancer metabolism to overcome therapeutic resistance. Cancer Res 2013; 73(9): 2709. https://doi.org/10.1158/0008-5472.CAN-12-3009.

41. Zong WX, Rabinowitz JD, White E. Mitochondria and cancer. Mol Cell 2016; 61(5): 667-76. https://doi.org/10.1016/j.molcel.2016.02.011.

42. Cantelmo AR, Conradi LC, Brajic A, Goveia J, Kalucka J, Pircher A, et al. Inhibition of the glycolytic activator pfkfb3 in endothelium induces tumor vessel normalization, impairs metastasis, and improves chemotherapy. Cancer Cell 2016; 30(6): 968-85. https://doi.org/10.1016/j.ccell.2016.10.006.

43. Vander HM, Cantley LC, Thompson CB. Understanding the warburg effect:

the metabolic requirements of cell proliferation. Science 2009; 324(5930): 1029-33. https://doi.org/10.1126/science.1160809.

44. Jia D, Park JH, Jung KH, Levine H, Kaipparettu BA. Elucidating the metabolic plasticity of cancer: mitochondrial reprogramming and hybrid metabolic states. Cells-Basel 2018; 7(3). https://doi.org/10.3390/cells7030021.

45. Sciacovelli M, Gonçalves E, Johnson TI, Zecchini VR, Da CA, Gaude E, et al. Fumarate is an epigenetic modifier that elicits epithelial-to-mesenchymal transition. Nature 2016; 537(7621): 544-7. https://doi.org/10.1038/nature19353.

46. Pathria P, Louis TL, Varner JA. Targeting tumor-associated macrophages in cancer. Trends Immunol 2019; 40(4): 310-27. https://doi.org/10.1016/j.it.2019.02.003.

47. Parra ER, Villalobos P, Behrens C, Jiang M, Pataer A, Swisher SG, et al. Effect of neoadjuvant chemotherapy on the immune microenvironment in non-small cell lung carcinomas as determined by multiplex immunofluorescence and image analysis approaches. J Immunother Cancer 2018; 6(1): 48. https://doi.org/10.1186/s40425-018-0368-0.

48. Talebian YM, Schinkelshoek MS, Loof NM, Taube C, Hiemstra PS, Welters MJ, et al. Standard radiotherapy but not chemotherapy impairs systemic immunity in non-small cell lung cancer. Oncoimmunology 2016; 5(12): e1255393. https://doi.org/10.1080/2162402X.2016.1255393.

Figure Legend

Figure 1. Single-cell atlas of lung adenocarcinoma (LUAD) tissues from the control, and NCT group. **(a)** Workflow depicting collection and processing of LUAD samples for scRNA-seq analysis. **(b)** Consensus clustering based on the correlations among the 20 clusters identified through the tSNE algorithm. **(c)** TSNE of the 83622 cells enrolled here, with each cell color indicating: its sample type of origin, the corresponding patient, predicted cell type, and the transcript counts. **(d)** Expression of marker genes for the cell types defined above each panel. **(e)** The proportion of each

cell type in different groups and samples. **(f)** For each of the eight epithelial subclusters and 43 non-epithelial clusters (left to right): the fraction of cells originating from the three groups, the fraction of cells originating from each of the nine patients, the number of cells and box plots of the number of transcripts (with plot center, box, and whiskers corresponding to the median, IQR and 1.5 × IQR, respectively). NCT: Neoadjuvant chemotherapy.

Figure 2. Metabolic reprogramming in lung adenocarcinoma driven by neoadjuvant chemotherapy. **(a)** The metabolic pathway activities of different cells from the Control group and NCT group showed significant differences. **(b)** The metabolic pathway activity of macrophages and malignant cells increased significantly after chemotherapy.

Figure 3. Tumor cells and epithelial cells had significant phenotypic changes before and after chemotherapy. **(a)** The tSNE plots and overview of the tumor cells and epithelial cells. **(b)** The proportion of malignant cells and nonmalignant cells in the Control group and NCT group. **(c)** Flow cytometry showed that the proportion of malignant cells was significantly reduced after chemotherapy and immunotherapy. **(d)** Marker genes of MalignantSA cells, MalignantNCT cells, MalignantPD cells, and Nonmalignant cells. **(e)** Pseudotime analysis showed that nonmalignant cells evolved in two directions. **(f)** The heat map showed that a series of genes play an important role in transforming epithelial cells into tumor cells. **(g)** GSVA analysis was performed for malignant and nonmalignant cells. **(h)** SCENIC analysis revealed the hub genes in the malignant transformation of epithelial cells. **(i)** The tSNE plots for re-clustered malignant cells. **(j)** Marker genes of 13 sub-clusters from malignant cells. **(k)** Metabolic characteristics in different malignant cell sub-clusters. **(l)** GSVA analysis reveals the characteristics of pathway activity in different malignant cell sub-clusters.

989 **Figure 4.** The scRNA profile of stromal cells derived from LUAD samples in control
990 and NCT groups. **(a)** The tSNE plots an overview of the 6 clusters of stromal cells.
991 **(b)** Proportions of the six predicted clusters of stromal cells in different groups and
992 samples. **(c)** Heatmap exhibiting the expression level of marker genes in each stromal
993 cell cluster. **(d)** GSVA analysis estimated the pathway activation levels of different
994 stromal cell subtypes. The scores have been normalized. **(e)** GSVA analysis revealed
995 the activation level of hallmark pathways in stromal cells (control vs. NCT groups) **(f)**
996 Heatmap exhibiting the expression level of marker genes in each fibroblast cluster. **(g-**
997 **h)** The tSNE plots revealed the group origins **(g)** and predicted subclusters **(h)** of
998 fibroblast. **(i-j)** GSVA analysis estivated the pathway activation levels of different
999 fibroblast subtypes.
1000
1001 **Figure 5.** Three newly identified subtypes of tumor-associated macrophages (TAMs)
1002 displayed distinct genetic and metabolic features. **(a)** The tSNE plots showed the
1003 group origins, sample origins, and clusters of TAMs. **(b)** Proportions of the 10 clusters
1004 of TAMs in different groups and samples. **(c)** Marker genes of the 10 clusters of
1005 TAMs. **(d)** GSVA analysis was performed for the 10 clusters of TAMs. **(e)** The
1006 activity of various metabolic processes in the 10 clusters of TAMs. **(f)** GSVA analysis
1007 was performed for TAMs from the Control group and NCT group. **(g)** SCENIC
1008 analysis was performed for the 10 clusters of TAMs. **(h)** Consensus clustering based
1009 on the correlations among the 10 clusters of TAMs identified through the tSNE
1010 algorithm. **(i)** Polarization score (left) and inflammatory score (right) for 10 clusters
1011 of TAMs based on the expression of polarization marker genes and inflammatory
1012 genes. **(j)** The tSNE plots for three types of TAMs. **(k)** Proportions of the three
1013 subtypes of TAMs in different groups and samples. **(l)** Development trajectory
1014 analysis for the three subtypes of TAMs. **(m)** Pseudotime analysis revealed a series of
1015 genes that affect the differentiation and development of macrophages.
1016
1017 **Figure 6.** Metabolic switching in tumor-associated macrophages (TAMs) contributed

1018 to diametrical effects on tumor cells. **(a)** The heatmap showed the essential marker
1019 genes for three subtypes of TAMs. **(b)** Based on Pro-mac and Anti-mac marker genes,
1020 these two types of cells were sorted by flow cytometry from lung adenocarcinoma
1021 tissue. **(c)** Flow cytometry verified the sorted cells. **(d)** The proportion changes of
1022 Pro-mac and Anti-mac cells in lung adenocarcinoma tissues before and after
1023 chemotherapy. **(e)** Immunofluorescence showed the changes in the proportion of
1024 TAMs with high CD206 and CD86 after neoadjuvant therapy. **(f)** The heatmap
1025 showed the differences in the cytokines secreted by the three subtypes of
1026 macrophages. **(g)** ELISA detected the secretion of VEGF, EGF, IL10, and MMP9. **(h)**
1027 The intensity of fluorescence changes in Luciferase-labeled A549 cells mixed with
1028 different TAMs. **(i)** The histogram showed the average fluorescence intensity emitted
1029 by the subcutaneous tumor. **(j)** GSVA analysis performed for Pro-mac, Anti-mac, and
1030 Mix. **(k)** Glucose uptake and lactate production in the TAMs cell subtypes. **(l)**
1031 Seahorse XFe96 cell outflow analyzer detected the glycolysis level of TAMs cell
1032 subtypes (Extracellular acidification rate: ECAR). **(m)** Transwell experiment detected
1033 the influence of TAMs subtypes on the invasion ability of A549 cells. **(n)** The 3D cell
1034 culture experiment detected the effect of 2-DG on the spheroidization ability of A549
1035 cells when cultured with subtypes of TAMs. **(o)** In vivo experiments verified the
1036 effect of 2-DG on the tumorigenesis ability of A549 after inhibiting glycolysis of
1037 TAMs. All error bars are mean ± SD. NS, not significant. ***$P < 0.001$, **$P < 0.01$,
1038 *$P < 0.05$; determined by two-tailed Student's t-test (95% confidence interval).
1039
1040 **Figure S1.** Figures related to Figure 1. **(a)** The tSNE plots of all clusters in this
1041 research. **(b)** The heatmap showed the marker genes in the different cell types.
1042
1043 **Figure S2.** Figures related to Figure 3. **(a)** Copy number variations (CNVs) of
1044 malignant and nonmalignant epithelial cells. **(b)** The proportion of malignant cells and
1045 nonmalignant cells from different patients. **(c)** The heatmap showed differentially

1046 expressed genes of epithelial cells in the Control group and NCT group. **(d)**
1047 Immunofluorescence showed LPCAT1, FOXL2, and RAC1 were highly expressed in
1048 normal lung tissues, the Control group, and the NCT group, respectively. **(e)** Some
1049 genes played an important role in the transformation of epithelial cells into tumor
1050 cells. **(f)** Changes in the activity of several important pathways during the
1051 transformation of epithelial cells to tumor cells. **(g)** The tSNE plots and overview of
1052 the non-malignant cells. **(h)** Heat map of marker genes for nonmalignant cells sub-
1053 clusters. **(i)** Metabolic characteristics in different nonmalignant cell sub-clusters. **(j)**
1054 GSVA analysis revealed the characteristics of pathway activity in different
1055 nonmalignant cell sub-clusters.
1056
1057 **Figure S3.** Figures related to Figure 4. **(a)** The activity of various metabolic processes
1058 in fibroblasts from the Control group and NCT group. **(b)** GSVA analysis was
1059 performed for fibroblasts from the Control group and NCT group. **(c)** SCENIC
1060 analysis revealed the hub genes in fibroblast.
1061
1062 **Figure S4.** The scRNA profile of B cells derived from LUAD samples in the control,
1063 neoadjuvant chemotherapy, and immunotherapy group. **(a)** The tSNE plots revealed
1064 the sample origins, group origins, and predicted clusters of B cells. **(b)** The two
1065 predicted clusters of B cells (plasma cells, class-switched memory B-cells) were
1066 reported in different groups and samples. **(c)** Heatmap exhibiting the expression level
1067 of marker genes in each B cell cluster. **(d)** GSVA analysis estivated the pathway

1068 activation levels of different B cell subtypes.

1069

1070 **Figure S5.** Crosstalk between cancer and immune cells. **(a)** Each cell type and the
1071 other cell types expressed some of the ligands. **(b)** Bubble plot revealing the specific
1072 ligand-receptor interactions between cancer cells and immune cells in the control
1073 group. The circle size indicates P values, with the scale to the right (permutation test),
1074 and color indicates communication probability.

1075

1076 **Figure S6.** The scRNA profile of T cells derived from LUAD samples in the control,
1077 neoadjuvant chemotherapy, and immunotherapy group. **(a-c)** The tSNE plots revealed
1078 the sample origins **(a)**, group origins **(b),** and predicted clusters **(c)** of T cells. **(d)** The
1079 three indicated clusters of T cells (CD4+ T, CD8+ T, and Tregs) were reported in
1080 different groups and samples. **(e)** Bubble plot exhibiting the expression level of
1081 marker genes in each T cell cluster. **(f-h)** The tSNE plots revealed the sample origins
1082 **(f)**, group origins **(g),** and predicted subclusters **(h)** of CD8+ T cells. **(i)** Heatmap
1083 exhibiting the expression level of marker genes corresponding to naïve,
1084 Treg/exhausted, and cytotoxic phenotypes in each CD8+ T cell subcluster. **(j-k)**
1085 Proportions of the five predicted clusters of CD8+ T cells in different samples **(j)** and
1086 groups **(k)**. **(l)** Dynamic changes in gene expression of CD8+ T cells during the
1087 transition (divided into three phases). **(m-p)** Pseudotime-ordered analysis of CD8+ T
1088 cells **(m-n)** revealing the dynamics of their cytotoxic **(o)** and exhausted levels **(p)**. **(l)**
1089 SCENIC analysis of CD8+ T cells.

1090

1091 **Figure S7.** Crosstalk between cancer and immune cells. **(a)** Overview of selected
1092 ligand-receptor interactions of cancer cells and immune cells in control and NCT
1093 groups. The line thickness indicates the number of ligands when cognate receptors are
1094 present in the recipient cell type. The loops indicate autocrine circuits. **(b)** Detailed
1095 view of the ligands expressed by each cell type and the other cell types. **(c)** Bubble
1096 plot revealing the specific ligand-receptor interactions between cancer cells and
1097 immune cells in the NCT group. The circle size indicates P values, with the scale to
1098 the right (permutation test), and color indicates communication probability.

1099

1100

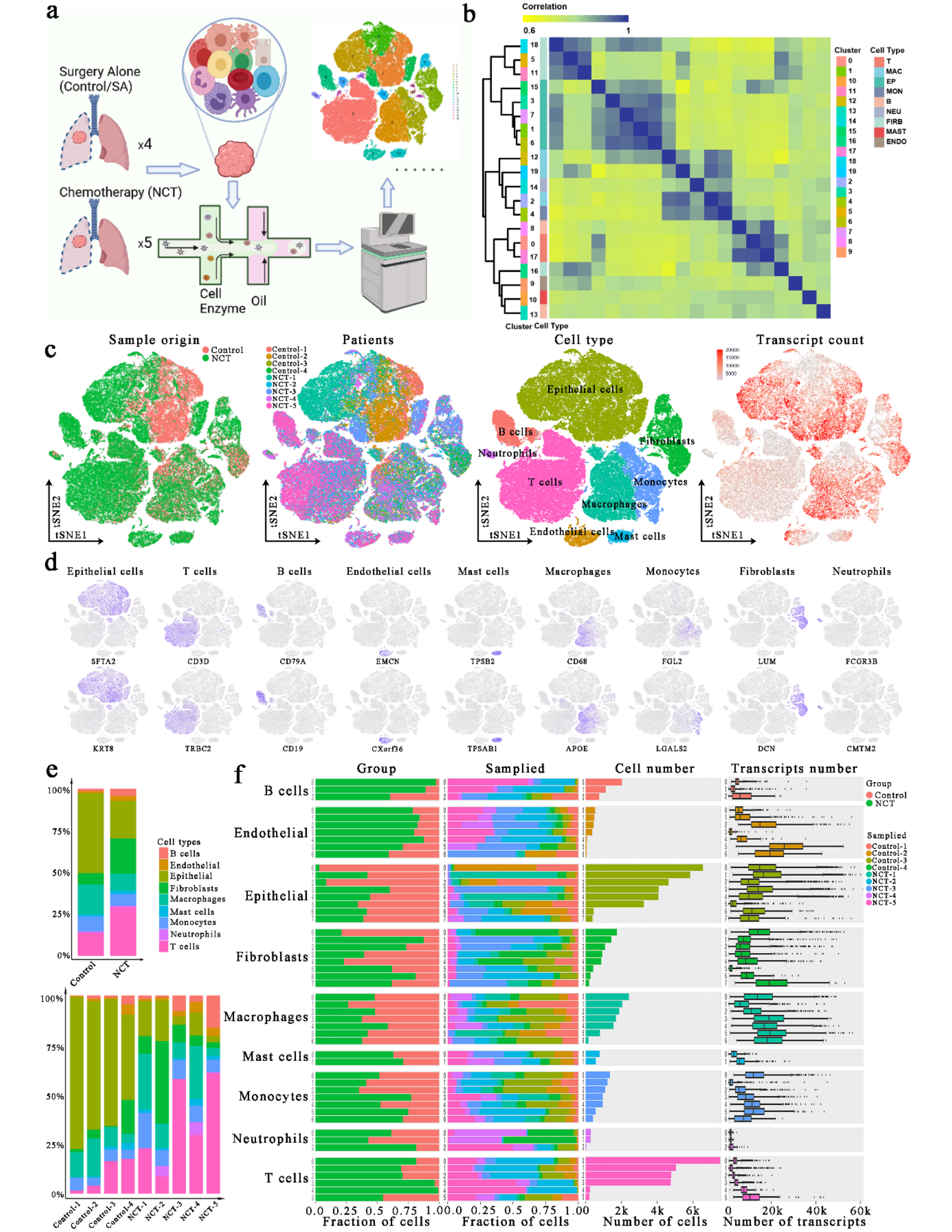
a
Surgery Alone
(Control/SA)
x4
Chemotherapy (NCT)
x5
Cell
Enzyme
Oil
b
Correlation
0.6
1
Cluster
Cell Type
T
MAC
EP
MON
B
NEU
FIRB
MAST
ENDO
Cluster Cell Type
c
Sample origin
Control
NCT
Patients
Control-1
Control-2
Control-3
Control-4
NCT-1
NCT-2
NCT-3
NCT-4
NCT-5
Cell type
Epithelial cells
B cells
Neutrophils
T cells
Fibroblasts
Monocytes
Macrophages
Endothelial cells
Mast cells
Transcript count
tSNE1
tSNE2
d
Epithelial cells
T cells
B cells
Endothelial cells
Mast cells
Macrophages
Monocytes
Fibroblasts
Neutrophils
SFTA2
CD3D
CD79A
EMCN
TPSB2
CD68
FGL2
LUM
FCGR3B
KRT8
TRBC2
CD19
CXorf36
TPSAB1
APOE
LGALS2
DCN
CMTM2
e
100%
75%
50%
25%
0%
Control
NCT
Cell types
B cells
Endothelial
Epithelial
Fibroblasts
Macrophages
Mast cells
Monocytes
Neutrophils
T cells
Control-1
Control-2
Control-3
Control-4
NCT-1
NCT-2
NCT-3
NCT-4
NCT-5
f
Group
Samplied
Cell number
Transcripts number
B cells
Endothelial
Epithelial
Fibroblasts
Macrophages
Mast cells
Monocytes
Neutrophils
T cells
Fraction of cells
Number of cells
Number of transcripts
0.0
0.25
0.5
0.75
1.00
2k
4k
6k
0
20k
40k
60k

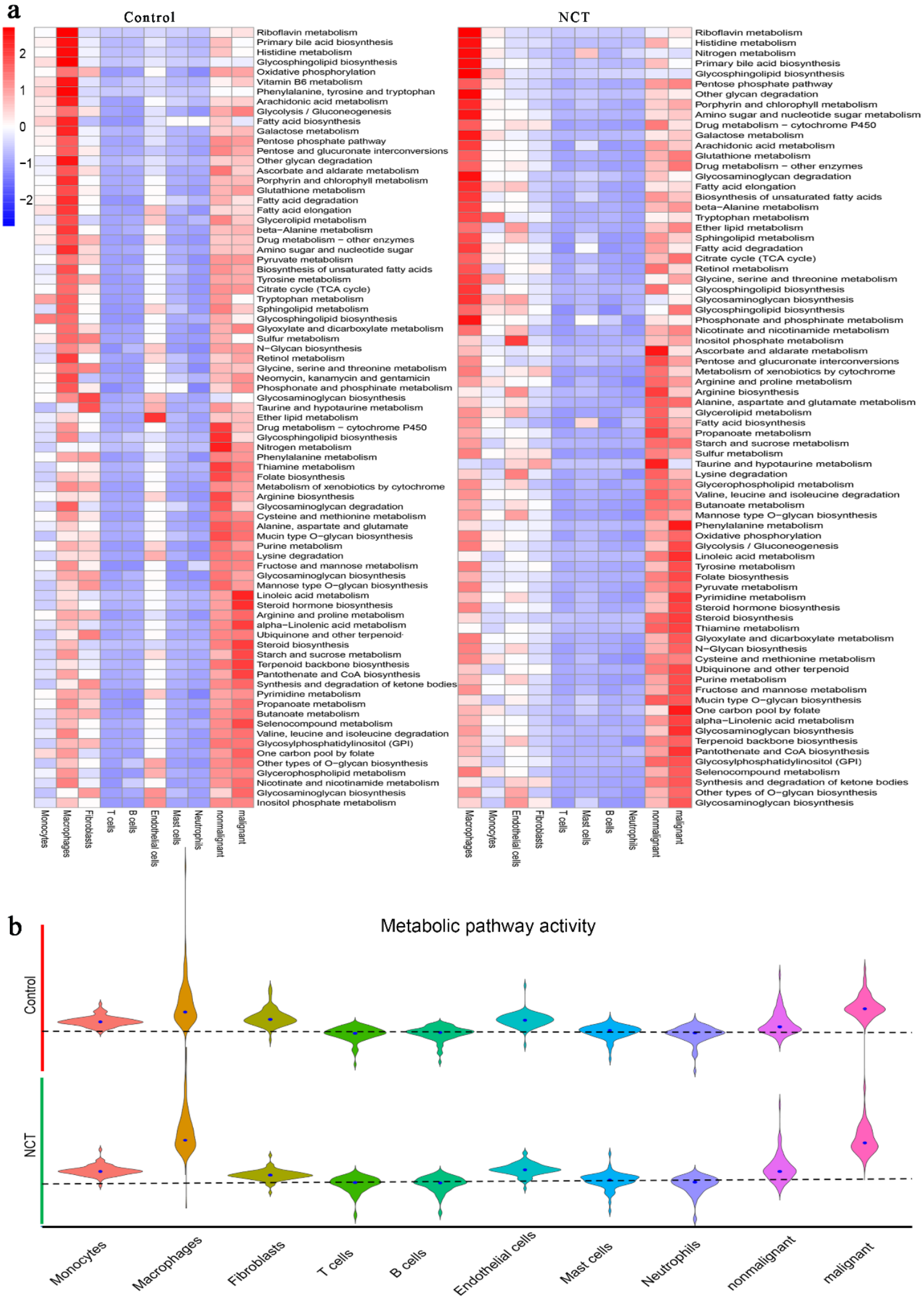
a
Control
NCT
2
1
0
−1
−2
Riboflavin metabolism
Primary bile acid biosynthesis
Histidine metabolism
Glycosphingolipid biosynthesis
Oxidative phosphorylation
Vitamin B6 metabolism
Phenylalanine, tyrosine and tryptophan
Arachidonic acid metabolism
Glycolysis / Gluconeogenesis
Fatty acid biosynthesis
Galactose metabolism
Pentose phosphate pathway
Pentose and glucuronate interconversions
Other glycan degradation
Ascorbate and aldarate metabolism
Porphyrin and chlorophyll metabolism
Glutathione metabolism
Fatty acid degradation
Fatty acid elongation
Glycerolipid metabolism
beta−Alanine metabolism
Drug metabolism − other enzymes
Amino sugar and nucleotide sugar
Pyruvate metabolism
Biosynthesis of unsaturated fatty acids
Tyrosine metabolism
Citrate cycle (TCA cycle)
Tryptophan metabolism
Sphingolipid metabolism
Glycosphingolipid biosynthesis
Glyoxylate and dicarboxylate metabolism
Sulfur metabolism
N−Glycan biosynthesis
Retinol metabolism
Glycine, serine and threonine metabolism
Neomycin, kanamycin and gentamicin
Phosphonate and phosphinate metabolism
Glycosaminoglycan biosynthesis
Taurine and hypotaurine metabolism
Ether lipid metabolism
Drug metabolism − cytochrome P450
Glycosphingolipid biosynthesis
Nitrogen metabolism
Phenylalanine metabolism
Thiamine metabolism
Folate biosynthesis
Metabolism of xenobiotics by cytochrome
Arginine biosynthesis
Glycosaminoglycan degradation
Cysteine and methionine metabolism
Alanine, aspartate and glutamate
Mucin type O−glycan biosynthesis
Purine metabolism
Lysine degradation
Fructose and mannose metabolism
Glycosaminoglycan biosynthesis
Mannose type O−glycan biosynthesis
Linoleic acid metabolism
Steroid hormone biosynthesis
Arginine and proline metabolism
alpha−Linolenic acid metabolism
Ubiquinone and other terpenoid·
Steroid biosynthesis
Starch and sucrose metabolism
Terpenoid backbone biosynthesis
Pantothenate and CoA biosynthesis
Synthesis and degradation of ketone bodies
Pyrimidine metabolism
Propanoate metabolism
Butanoate metabolism
Selenocompound metabolism
Valine, leucine and isoleucine degradation
Glycosylphosphatidylinositol (GPI)
One carbon pool by folate
Other types of O−glycan biosynthesis
Glycerophospholipid metabolism
Nicotinate and nicotinamide metabolism
Glycosaminoglycan biosynthesis
Inositol phosphate metabolism
Monocytes
Macrophages
Fibroblasts
T cells
B cells
Endothelial cells
Mast cells
Neutrophils
nonmalignant
malignant
Riboflavin metabolism
Histidine metabolism
Nitrogen metabolism
Primary bile acid biosynthesis
Glycosphingolipid biosynthesis
Pentose phosphate pathway
Other glycan degradation
Porphyrin and chlorophyll metabolism
Amino sugar and nucleotide sugar metabolism
Drug metabolism − cytochrome P450
Galactose metabolism
Arachidonic acid metabolism
Glutathione metabolism
Drug metabolism − other enzymes
Glycosaminoglycan degradation
Fatty acid elongation
Biosynthesis of unsaturated fatty acids
beta−Alanine metabolism
Tryptophan metabolism
Ether lipid metabolism
Sphingolipid metabolism
Fatty acid degradation
Citrate cycle (TCA cycle)
Retinol metabolism
Glycine, serine and threonine metabolism
Glycosphingolipid biosynthesis
Glycosaminoglycan biosynthesis
Glycosphingolipid biosynthesis
Phosphonate and phosphinate metabolism
Nicotinate and nicotinamide metabolism
Inositol phosphate metabolism
Ascorbate and aldarate metabolism
Pentose and glucuronate interconversions
Metabolism of xenobiotics by cytochrome
Arginine and proline metabolism
Arginine biosynthesis
Alanine, aspartate and glutamate metabolism
Glycerolipid metabolism
Fatty acid biosynthesis
Propanoate metabolism
Starch and sucrose metabolism
Sulfur metabolism
Taurine and hypotaurine metabolism
Lysine degradation
Glycerophospholipid metabolism
Valine, leucine and isoleucine degradation
Butanoate metabolism
Mannose type O−glycan biosynthesis
Phenylalanine metabolism
Oxidative phosphorylation
Glycolysis / Gluconeogenesis
Linoleic acid metabolism
Tyrosine metabolism
Folate biosynthesis
Pyruvate metabolism
Pyrimidine metabolism
Steroid hormone biosynthesis
Steroid biosynthesis
Thiamine metabolism
Glyoxylate and dicarboxylate metabolism
N−Glycan biosynthesis
Cysteine and methionine metabolism
Ubiquinone and other terpenoid
Purine metabolism
Fructose and mannose metabolism
Mucin type O−glycan biosynthesis
One carbon pool by folate
alpha−Linolenic acid metabolism
Glycosaminoglycan biosynthesis
Terpenoid backbone biosynthesis
Pantothenate and CoA biosynthesis
Glycosylphosphatidylinositol (GPI)
Selenocompound metabolism
Synthesis and degradation of ketone bodies
Other types of O−glycan biosynthesis
Glycosaminoglycan biosynthesis
Macrophages
Monocytes
Endothelial cells
Fibroblasts
T cells
Mast cells
B cells
Neutrophils
nonmalignant
malignant
b
Metabolic pathway activity
Control
NCT
Monocytes
Macrophages
Fibroblasts
T cells
B cells
Endothelial cells
Mast cells
Neutrophils
nonmalignant
malignant

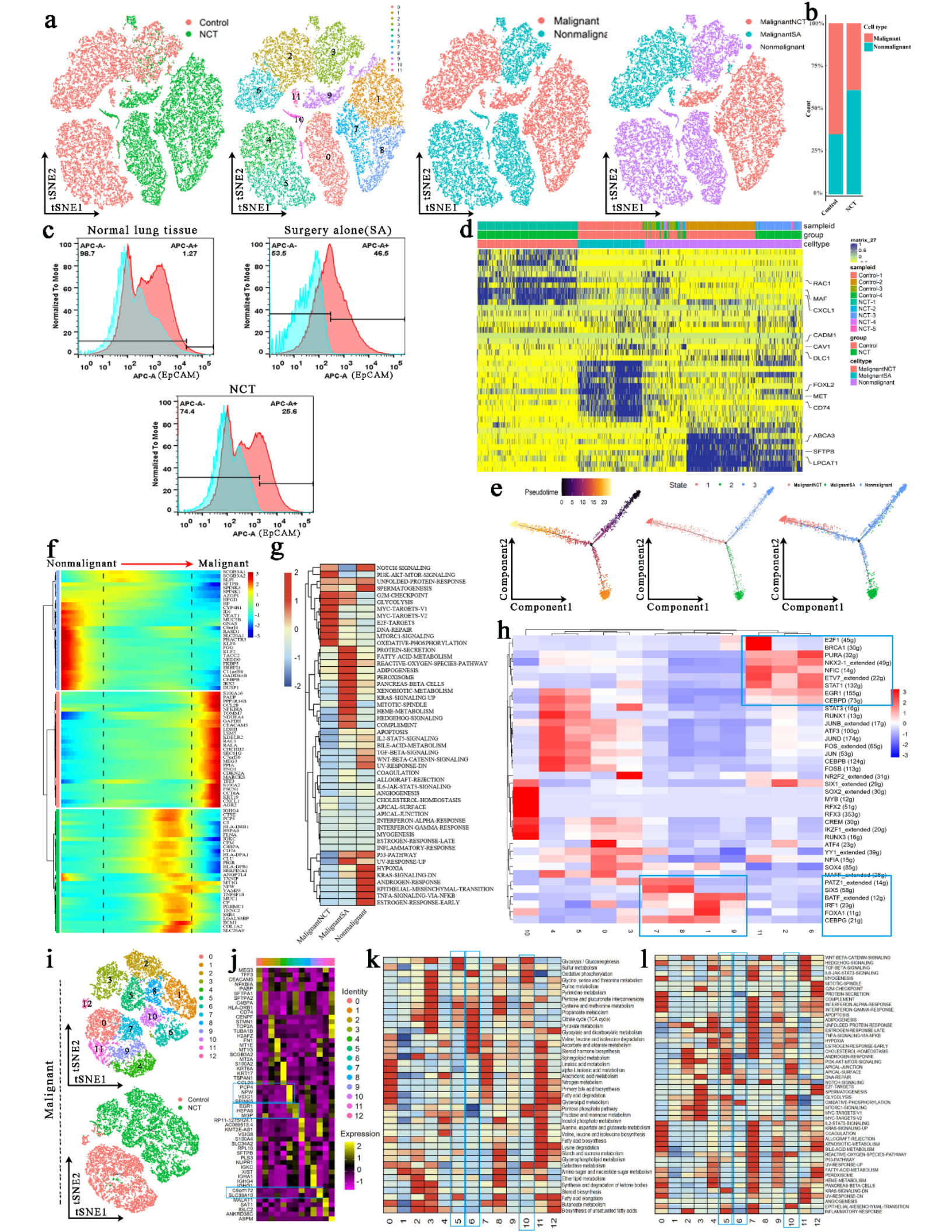
a
Control
NCT
Malignant
Nonmalignant
MalignantNCT
MalignantSA
Nonmalignant
tSNE1
tSNE2
b
Cell type
Malignant
Nonmalignant
Count
Control
NCT
c
Normal lung tissue
APC-A- 98.7
APC-A+ 1.27
Surgery alone(SA)
APC-A- 53.5
APC-A+ 46.5
NCT
APC-A- 74.4
APC-A+ 25.6
Normalized To Mode
APC-A (EpCAM)
d
sampleid
group
celltype
RAC1
MAF
CXCL1
CADM1
CAV1
DLC1
FOXL2
MET
CD74
ABCA3
SFTPB
LPCAT1
e
Pseudotime
State
Component1
Component2
f
Nonmalignant
Malignant
g
NOTCH-SIGNALING
PI3K-AKT-MTOR-SIGNALING
UNFOLDED-PROTEIN-RESPONSE
SPERMATOGENESIS
G2M-CHECKPOINT
GLYCOLYSIS
MYC-TARGETS-V1
MYC-TARGETS-V2
E2F-TARGETS
DNA-REPAIR
MTORC1-SIGNALING
OXIDATIVE-PHOSPHORYLATION
PROTEIN-SECRETION
FATTY-ACID-METABOLISM
REACTIVE-OXYGEN-SPECIES-PATHWAY
ADIPOGENESIS
PEROXISOME
PANCREAS-BETA-CELLS
XENOBIOTIC-METABOLISM
KRAS-SIGNALING-UP
MITOTIC-SPINDLE
HEME-METABOLISM
HEDGEHOG-SIGNALING
COMPLEMENT
APOPTOSIS
IL2-STAT5-SIGNALING
BILE-ACID-METABOLISM
TGF-BETA-SIGNALING
WNT-BETA-CATENIN-SIGNALING
UV-RESPONSE-DN
COAGULATION
ALLOGRAFT-REJECTION
IL6-JAK-STAT3-SIGNALING
ANGIOGENESIS
CHOLESTEROL-HOMEOSTASIS
APICAL-SURFACE
APICAL-JUNCTION
INTERFERON-ALPHA-RESPONSE
INTERFERON-GAMMA-RESPONSE
MYOGENESIS
ESTROGEN-RESPONSE-LATE
INFLAMMATORY-RESPONSE
P53-PATHWAY
UV-RESPONSE-UP
HYPOXIA
KRAS-SIGNALING-DN
ANDROGEN-RESPONSE
EPITHELIAL-MESENCHYMAL-TRANSITION
TNFA-SIGNALING-VIA-NFKB
ESTROGEN-RESPONSE-EARLY
MalignantNCT
MalignantSA
Nonmalignant
h
E2F1 (45g)
BRCA1 (30g)
PURA (32g)
NKX2-1_extended (49g)
NFIC (14g)
ETV7_extended (22g)
STAT1 (132g)
EGR1 (55g)
CEBPD (73g)
STAT3 (16g)
RUNX1 (13g)
JUNB_extended (17g)
ATF3 (100g)
JUND (174g)
FOS_extended (65g)
JUN (53g)
CEBPB (124g)
FOSB (113g)
NR2F2_extended (31g)
SIX1_extended (29g)
SOX2_extended (30g)
MYB (12g)
RFX2 (51g)
RFX3 (353g)
CREM (30g)
IKZF1_extended (20g)
RUNX3 (16g)
ATF4 (23g)
YY1_extended (39g)
NFIA (15g)
SOX4 (85g)
MAFF_extended (28g)
PATZ1_extended (14g)
SIX5 (58g)
BATF_extended (12g)
IRF1 (23g)
FOXA1 (11g)
CEBPG (21g)
i
Malignant
Control
NCT
tSNE1
tSNE2
j
Identity
Expression
k
l

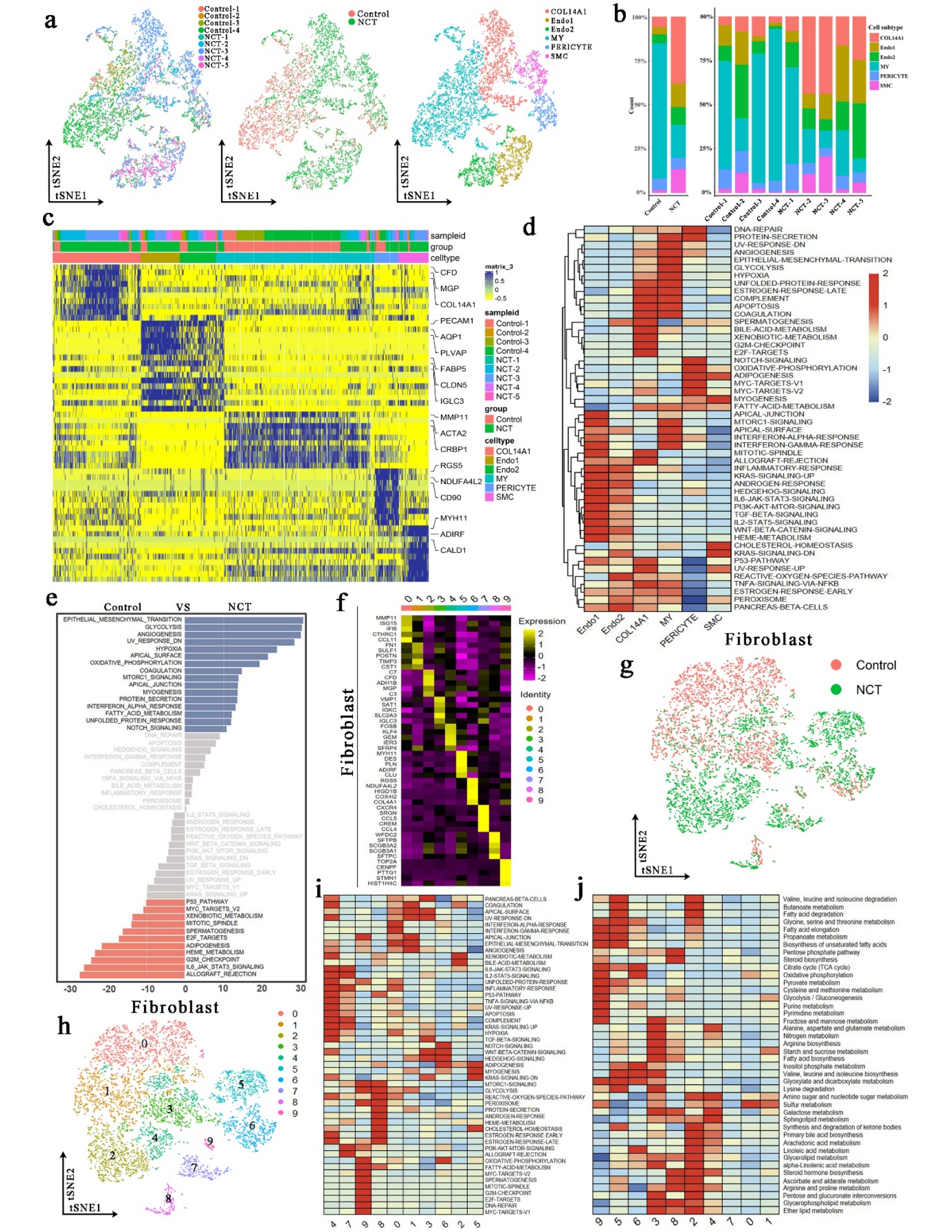
a
Control-1
Control-2
Control-3
Control-4
NCT-1
NCT-2
NCT-3
NCT-4
NCT-5
Control
NCT
COL14A1
Endo1
Endo2
MY
PERICYTE
SMC
tSNE1
tSNE2
b
Count
Cell subtype
c
sampleid
group
celltype
matrix_3
CFD
MGP
COL14A1
PECAM1
AQP1
PLVAP
FABP5
CLDN5
IGLC3
MMP11
ACTA2
CRBP1
RGS5
NDUFA4L2
CD90
MYH11
ADIRF
CALD1
d
DNA-REPAIR
PROTEIN-SECRETION
UV-RESPONSE-DN
ANGIOGENESIS
EPITHELIAL-MESENCHYMAL-TRANSITION
GLYCOLYSIS
HYPOXIA
UNFOLDED-PROTEIN-RESPONSE
ESTROGEN-RESPONSE-LATE
COMPLEMENT
APOPTOSIS
COAGULATION
SPERMATOGENESIS
BILE-ACID-METABOLISM
XENOBIOTIC-METABOLISM
G2M-CHECKPOINT
E2F-TARGETS
NOTCH-SIGNALING
OXIDATIVE-PHOSPHORYLATION
ADIPOGENESIS
MYC-TARGETS-V1
MYC-TARGETS-V2
MYOGENESIS
FATTY-ACID-METABOLISM
APICAL-JUNCTION
MTORC1-SIGNALING
APICAL-SURFACE
INTERFERON-ALPHA-RESPONSE
INTERFERON-GAMMA-RESPONSE
MITOTIC-SPINDLE
ALLOGRAFT-REJECTION
INFLAMMATORY-RESPONSE
KRAS-SIGNALING-UP
ANDROGEN-RESPONSE
HEDGEHOG-SIGNALING
IL6-JAK-STAT3-SIGNALING
PI3K-AKT-MTOR-SIGNALING
TGF-BETA-SIGNALING
IL2-STAT5-SIGNALING
WNT-BETA-CATENIN-SIGNALING
HEME-METABOLISM
CHOLESTEROL-HOMEOSTASIS
KRAS-SIGNALING-DN
P53-PATHWAY
UV-RESPONSE-UP
REACTIVE-OXYGEN-SPECIES-PATHWAY
TNFA-SIGNALING-VIA-NFKB
ESTROGEN-RESPONSE-EARLY
PEROXISOME
PANCREAS-BETA-CELLS
Endo1
Endo2
COL14A1
MY
PERICYTE
SMC
Fibroblast
e
Control VS NCT
Fibroblast
f
Expression
Identity
Fibroblast
g
Control
NCT
tSNE1
tSNE2
h
tSNE1
tSNE2
i
j

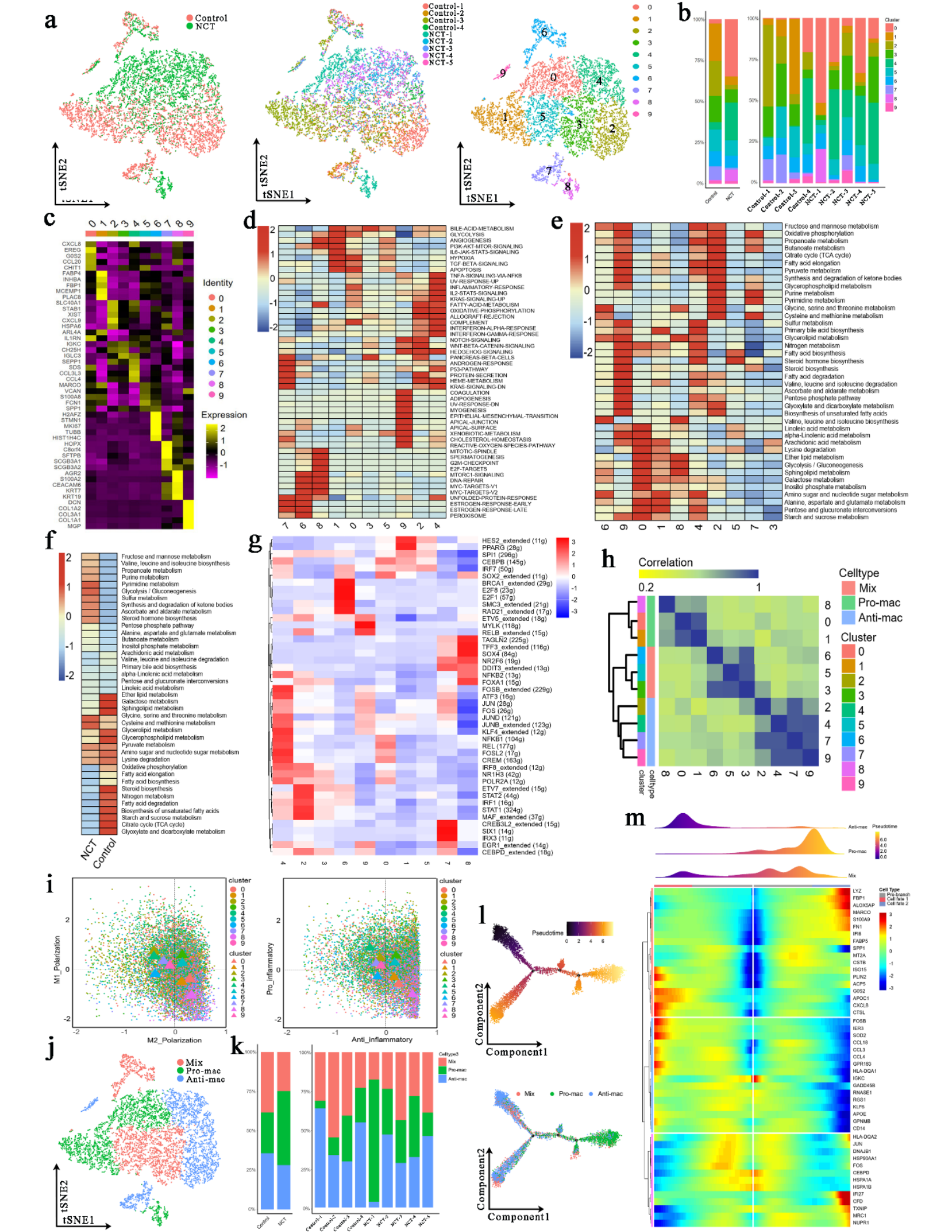
a
Control
NCT
tSNE2
tSNE1
Control-1
Control-2
Control-3
Control-4
NCT-1
NCT-2
NCT-3
NCT-4
NCT-5
b
Cluster
c
Identity
Expression
d
e
f
NCT
Control
g
h
Correlation
Celltype
Mix
Pro-mac
Anti-mac
Cluster
i
M1_Polarization
M2_Polarization
Pro_inflammatory
Anti_inflammatory
j
k
l
Pseudotime
Component1
Component2
m
Anti-mac
Pro-mac
Mix
Cell Type

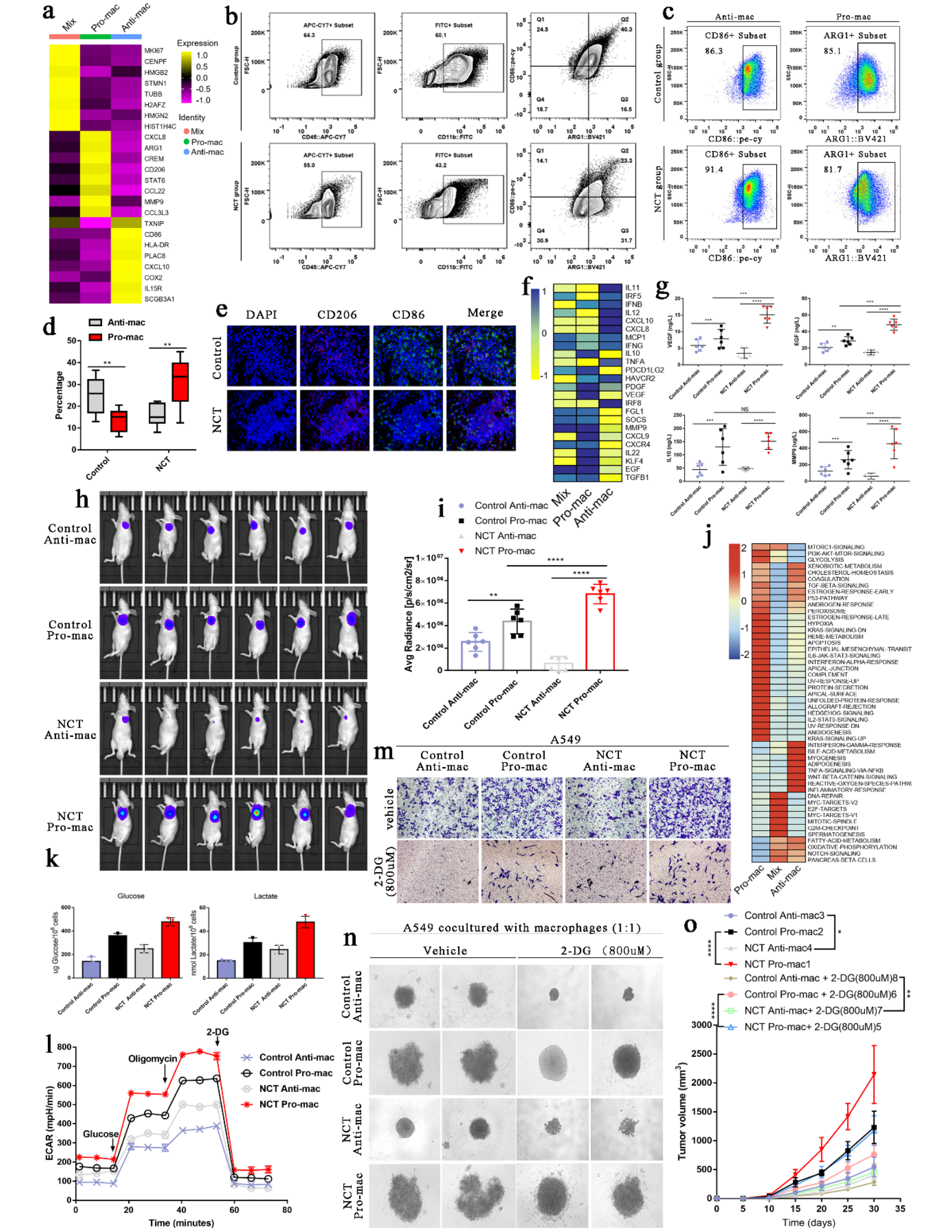
a
Mix
Pro-mac
Anti-mac
Expression
Identity
Mix
Pro-mac
Anti-mac
MKI67
CENPF
HMGB2
STMN1
TUBB
H2AFZ
HMGN2
HIST1H4C
CXCL8
ARG1
CREM
CD206
STAT6
CCL22
MMP9
CCL3L3
TXNIP
CD86
HLA-DR
PLAC8
CXCL10
COX2
IL15R
SCGB3A1
b
Control group
NCT group
APC-CY7+ Subset
FITC+ Subset
c
Anti-mac
Pro-mac
CD86+ Subset
ARG1+ Subset
d
Anti-mac
Pro-mac
Percentage
Control
NCT
e
DAPI
CD206
CD86
Merge
Control
NCT
f
IL11
IRF5
IFNB
IL12
CXCL10
CXCL8
MCP1
IFNG
IL10
TNFA
PDCD1LG2
HAVCR2
PDGF
VEGF
IRF8
FGL1
SOCS
MMP9
CXCL9
CXCR4
IL22
KLF4
EGF
TGFB1
Mix
Pro-mac
Anti-mac
g
VEGF (ng/L)
EGF (ng/L)
IL10 (ng/L)
MMP9 (ug/L)
Control Anti-mac
Control Pro-mac
NCT Anti-mac
NCT Pro-mac
h
Control Anti-mac
Control Pro-mac
NCT Anti-mac
NCT Pro-mac
i
Control Anti-mac
Control Pro-mac
NCT Anti-mac
NCT Pro-mac
Avg Radiance [p/s/cm2/sr]
j
MTORC1-SIGNALING
PI3K-AKT-MTOR-SIGNALING
GLYCOLYSIS
XENOBIOTIC-METABOLISM
CHOLESTEROL-HOMEOSTASIS
COAGULATION
TGF-BETA-SIGNALING
ESTROGEN-RESPONSE-EARLY
P53-PATHWAY
ANDROGEN-RESPONSE
PEROXISOME
ESTROGEN-RESPONSE-LATE
HYPOXIA
KRAS-SIGNALING-DN
HEME-METABOLISM
APOPTOSIS
EPITHELIAL-MESENCHYMAL-TRANSIT
IL6-JAK-STAT3-SIGNALING
INTERFERON-ALPHA-RESPONSE
APICAL-JUNCTION
COMPLEMENT
UV-RESPONSE-UP
PROTEIN-SECRETION
APICAL-SURFACE
UNFOLDED-PROTEIN-RESPONSE
ALLOGRAFT-REJECTION
HEDGEHOG-SIGNALING
IL2-STAT5-SIGNALING
UV-RESPONSE-DN
ANGIOGENESIS
KRAS-SIGNALING-UP
INTERFERON-GAMMA-RESPONSE
BILE-ACID-METABOLISM
MYOGENESIS
ADIPOGENESIS
TNFA-SIGNALING-VIA-NFKB
WNT-BETA-CATENIN-SIGNALING
REACTIVE-OXYGEN-SPECIES-PATHW
INFLAMMATORY-RESPONSE
DNA-REPAIR
MYC-TARGETS-V2
E2F-TARGETS
MYC-TARGETS-V1
MITOTIC-SPINDLE
G2M-CHECKPOINT
SPERMATOGENESIS
FATTY-ACID-METABOLISM
OXIDATIVE-PHOSPHORYLATION
NOTCH-SIGNALING
PANCREAS-BETA-CELLS
Pro-mac
Mix
Anti-mac
k
Glucose
Lactate
ug Glucose/10^6 cells
nmol Lactate/10^6 cells
Control Anti-mac
Control Pro-mac
NCT Anti-mac
NCT Pro-mac
l
2-DG
Oligomycin
Glucose
ECAR (mpH/min)
Time (minutes)
Control Anti-mac
Control Pro-mac
NCT Anti-mac
NCT Pro-mac
m
A549
Control Anti-mac
Control Pro-mac
NCT Anti-mac
NCT Pro-mac
vehicle
2-DG (800uM)
n
A549 cocultured with macrophages (1:1)
Vehicle
2-DG (800uM)
Control Anti-mac
Control Pro-mac
NCT Anti-mac
NCT Pro-mac
o
Control Anti-mac3
Control Pro-mac2
NCT Anti-mac4
NCT Pro-mac1
Control Anti-mac + 2-DG(800uM)8
Control Pro-mac + 2-DG(800uM)6
NCT Anti-mac+ 2-DG(800uM)7
NCT Pro-mac+ 2-DG(800uM)5
Tumor volume (mm3)
Time (days)

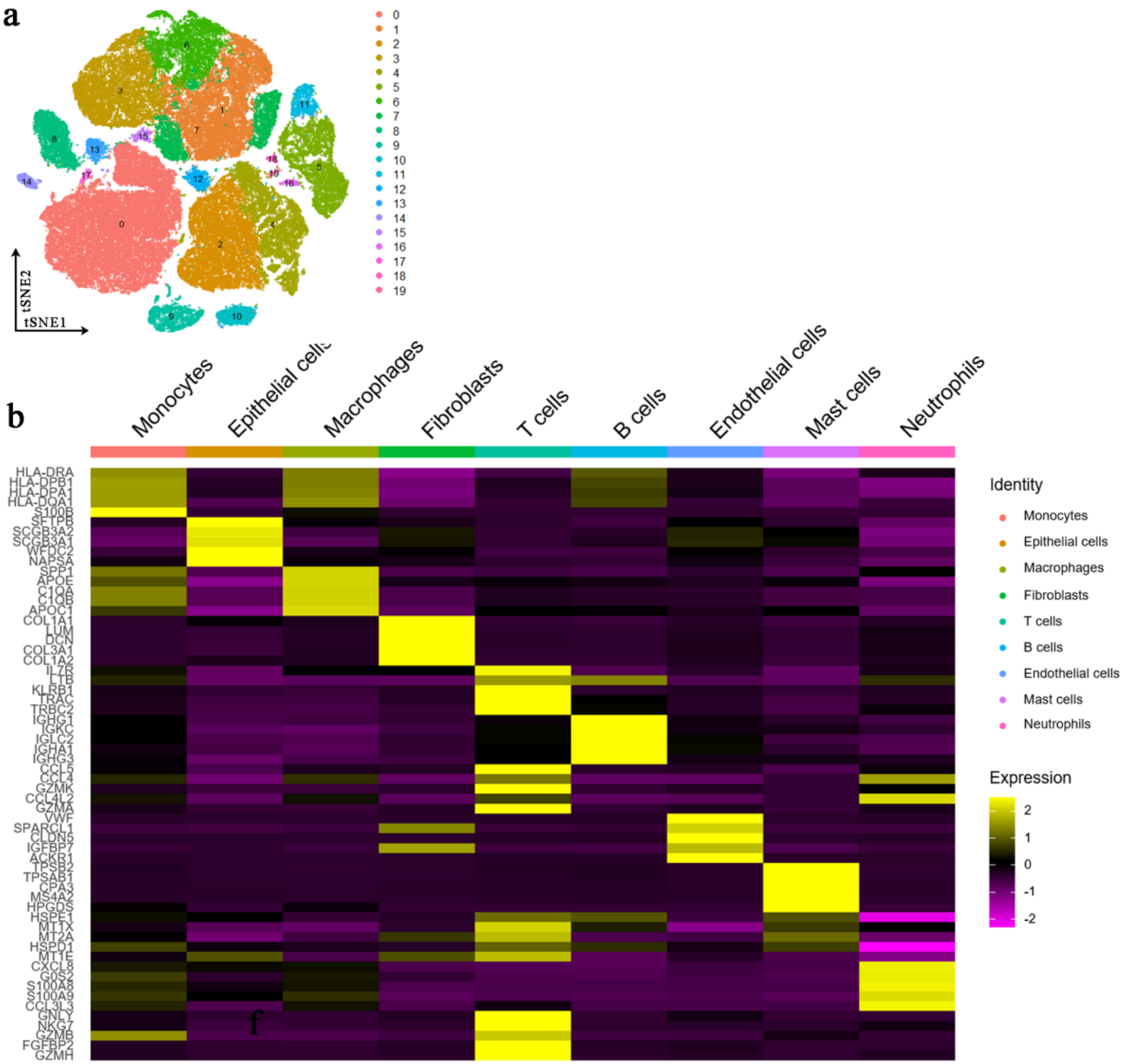
a
tSNE2
tSNE1
0
1
2
3
4
5
6
7
8
9
10
11
12
13
14
15
16
17
18
19
b
Monocytes
Epithelial cells
Macrophages
Fibroblasts
T cells
B cells
Endothelial cells
Mast cells
Neutrophils
HLA-DRA
HLA-DPB1
HLA-DPA1
HLA-DQA1
S100B
SFTPB
SCGB3A2
SCGB3A1
WFDC2
NAPSA
SPP1
APOE
C1QA
C1QB
APOC1
COL1A1
LUM
DCN
COL3A1
COL1A2
IL7R
LTB
KLRB1
TRAC
TRBC2
IGHG1
IGKC
IGLC2
IGHA1
IGHG3
CCL5
CCL4
GZMK
CCL4L2
GZMA
VWF
SPARCL1
CLDN5
IGFBP7
ACKR1
TPSB2
TPSAB1
CPA3
MS4A2
HPGDS
HSPE1
MT1X
MT2A
HSPD1
MT1E
CXCL8
G0S2
S100A8
S100A9
CCL3L3
GNLY
NKG7
GZMB
FGFBP2
GZMH
Identity
Monocytes
Epithelial cells
Macrophages
Fibroblasts
T cells
B cells
Endothelial cells
Mast cells
Neutrophils
Expression
2
1
0
-1
-2

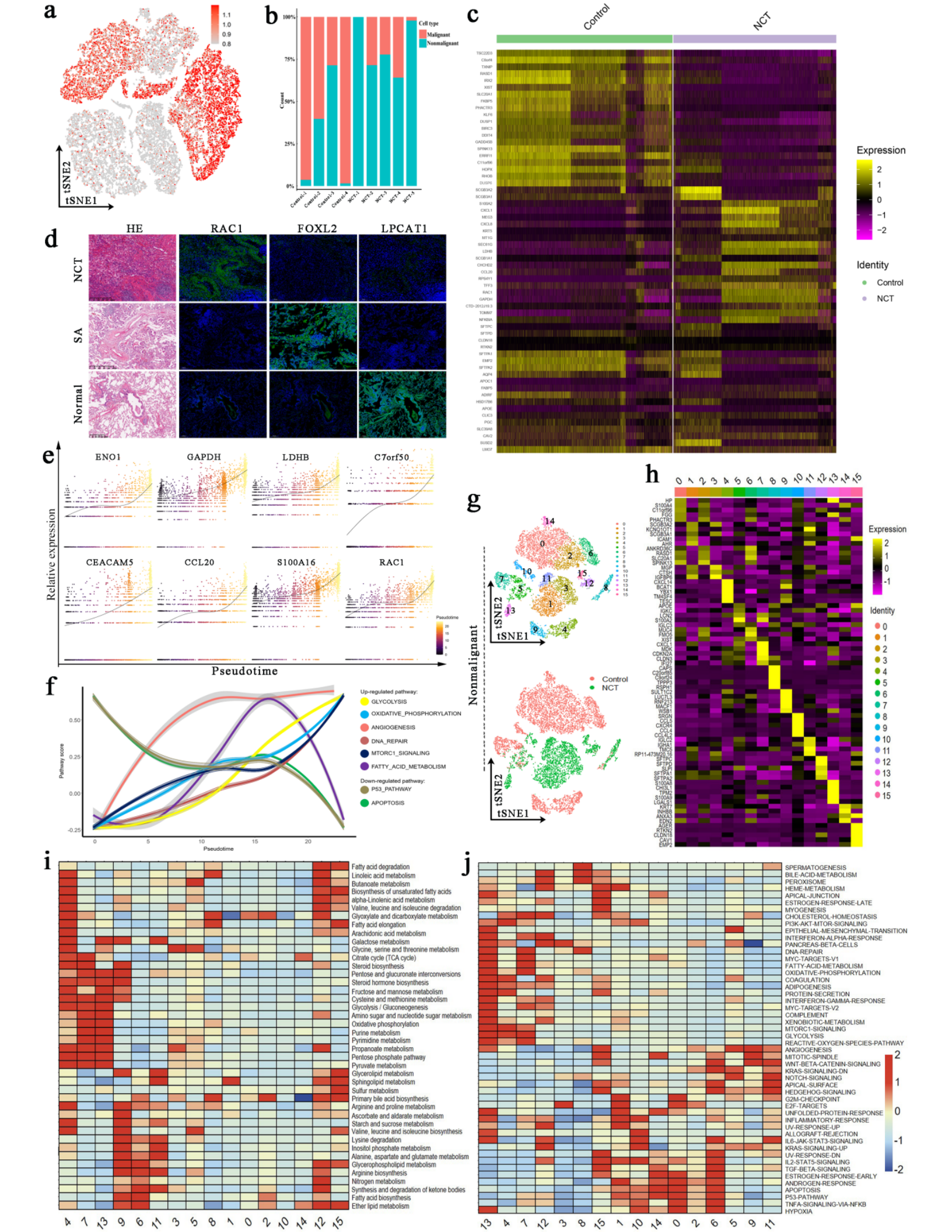
a
tSNE2
tSNE1
b
Cell type
Malignant
Nonmalignant
Count
c
Control
NCT
Expression
Identity
Control
NCT
d
HE
RAC1
FOXL2
LPCAT1
NCT
SA
Normal
e
ENO1
GAPDH
LDHB
C7orf50
CEACAM5
CCL20
S100A16
RAC1
Relative expression
Pseudotime
f
Up-regulated pathway:
GLYCOLYSIS
OXIDATIVE_PHOSPHORYLATION
ANGIOGENESIS
DNA_REPAIR
MTORC1_SIGNALING
FATTY_ACID_METABOLISM
Down-regulated pathway:
P53_PATHWAY
APOPTOSIS
Pathway score
Pseudotime
g
Nonmalignant
tSNE2
tSNE1
Control
NCT
h
Expression
Identity
i
Fatty acid degradation
Linoleic acid metabolism
Butanoate metabolism
Biosynthesis of unsaturated fatty acids
alpha-Linolenic acid metabolism
Valine, leucine and isoleucine degradation
Glyoxylate and dicarboxylate metabolism
Fatty acid elongation
Arachidonic acid metabolism
Galactose metabolism
Glycine, serine and threonine metabolism
Citrate cycle (TCA cycle)
Steroid biosynthesis
Pentose and glucuronate interconversions
Steroid hormone biosynthesis
Fructose and mannose metabolism
Cysteine and methionine metabolism
Glycolysis / Gluconeogenesis
Amino sugar and nucleotide sugar metabolism
Oxidative phosphorylation
Purine metabolism
Pyrimidine metabolism
Propanoate metabolism
Pentose phosphate pathway
Pyruvate metabolism
Glycerolipid metabolism
Sphingolipid metabolism
Sulfur metabolism
Primary bile acid biosynthesis
Arginine and proline metabolism
Ascorbate and aldarate metabolism
Starch and sucrose metabolism
Valine, leucine and isoleucine biosynthesis
Lysine degradation
Inositol phosphate metabolism
Alanine, aspartate and glutamate metabolism
Glycerophospholipid metabolism
Arginine biosynthesis
Nitrogen metabolism
Synthesis and degradation of ketone bodies
Fatty acid biosynthesis
Ether lipid metabolism
j
SPERMATOGENESIS
BILE-ACID-METABOLISM
PEROXISOME
HEME-METABOLISM
APICAL-JUNCTION
ESTROGEN-RESPONSE-LATE
MYOGENESIS
CHOLESTEROL-HOMEOSTASIS
PI3K-AKT-MTOR-SIGNALING
EPITHELIAL-MESENCHYMAL-TRANSITION
INTERFERON-ALPHA-RESPONSE
PANCREAS-BETA-CELLS
DNA-REPAIR
MYC-TARGETS-V1
FATTY-ACID-METABOLISM
OXIDATIVE-PHOSPHORYLATION
COAGULATION
ADIPOGENESIS
PROTEIN-SECRETION
INTERFERON-GAMMA-RESPONSE
MYC-TARGETS-V2
COMPLEMENT
XENOBIOTIC-METABOLISM
MTORC1-SIGNALING
GLYCOLYSIS
REACTIVE-OXYGEN-SPECIES-PATHWAY
ANGIOGENESIS
MITOTIC-SPINDLE
WNT-BETA-CATENIN-SIGNALING
KRAS-SIGNALING-DN
NOTCH-SIGNALING
APICAL-SURFACE
HEDGEHOG-SIGNALING
G2M-CHECKPOINT
E2F-TARGETS
UNFOLDED-PROTEIN-RESPONSE
INFLAMMATORY-RESPONSE
UV-RESPONSE-UP
ALLOGRAFT-REJECTION
IL6-JAK-STAT3-SIGNALING
KRAS-SIGNALING-UP
UV-RESPONSE-DN
IL2-STAT5-SIGNALING
TGF-BETA-SIGNALING
ESTROGEN-RESPONSE-EARLY
ANDROGEN-RESPONSE
APOPTOSIS
P53-PATHWAY
TNFA-SIGNALING-VIA-NFKB
HYPOXIA

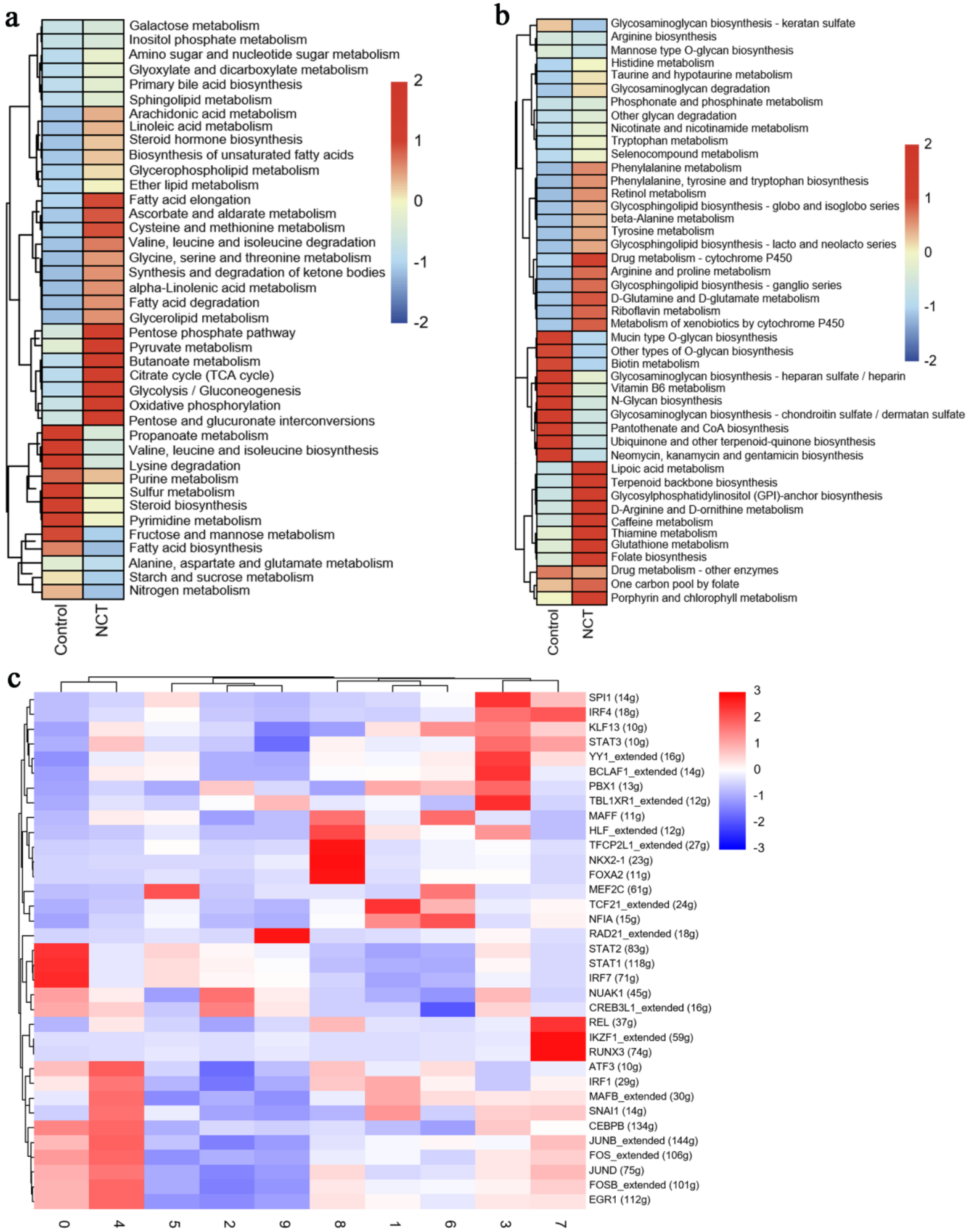
a
Galactose metabolism
Inositol phosphate metabolism
Amino sugar and nucleotide sugar metabolism
Glyoxylate and dicarboxylate metabolism
Primary bile acid biosynthesis
Sphingolipid metabolism
Arachidonic acid metabolism
Linoleic acid metabolism
Steroid hormone biosynthesis
Biosynthesis of unsaturated fatty acids
Glycerophospholipid metabolism
Ether lipid metabolism
Fatty acid elongation
Ascorbate and aldarate metabolism
Cysteine and methionine metabolism
Valine, leucine and isoleucine degradation
Glycine, serine and threonine metabolism
Synthesis and degradation of ketone bodies
alpha-Linolenic acid metabolism
Fatty acid degradation
Glycerolipid metabolism
Pentose phosphate pathway
Pyruvate metabolism
Butanoate metabolism
Citrate cycle (TCA cycle)
Glycolysis / Gluconeogenesis
Oxidative phosphorylation
Pentose and glucuronate interconversions
Propanoate metabolism
Valine, leucine and isoleucine biosynthesis
Lysine degradation
Purine metabolism
Sulfur metabolism
Steroid biosynthesis
Pyrimidine metabolism
Fructose and mannose metabolism
Fatty acid biosynthesis
Alanine, aspartate and glutamate metabolism
Starch and sucrose metabolism
Nitrogen metabolism
Control
NCT
2
1
0
-1
-2
b
Glycosaminoglycan biosynthesis - keratan sulfate
Arginine biosynthesis
Mannose type O-glycan biosynthesis
Histidine metabolism
Taurine and hypotaurine metabolism
Glycosaminoglycan degradation
Phosphonate and phosphinate metabolism
Other glycan degradation
Nicotinate and nicotinamide metabolism
Tryptophan metabolism
Selenocompound metabolism
Phenylalanine metabolism
Phenylalanine, tyrosine and tryptophan biosynthesis
Retinol metabolism
Glycosphingolipid biosynthesis - globo and isoglobo series
beta-Alanine metabolism
Tyrosine metabolism
Glycosphingolipid biosynthesis - lacto and neolacto series
Drug metabolism - cytochrome P450
Arginine and proline metabolism
Glycosphingolipid biosynthesis - ganglio series
D-Glutamine and D-glutamate metabolism
Riboflavin metabolism
Metabolism of xenobiotics by cytochrome P450
Mucin type O-glycan biosynthesis
Other types of O-glycan biosynthesis
Biotin metabolism
Glycosaminoglycan biosynthesis - heparan sulfate / heparin
Vitamin B6 metabolism
N-Glycan biosynthesis
Glycosaminoglycan biosynthesis - chondroitin sulfate / dermatan sulfate
Pantothenate and CoA biosynthesis
Ubiquinone and other terpenoid-quinone biosynthesis
Neomycin, kanamycin and gentamicin biosynthesis
Lipoic acid metabolism
Terpenoid backbone biosynthesis
Glycosylphosphatidylinositol (GPI)-anchor biosynthesis
D-Arginine and D-ornithine metabolism
Caffeine metabolism
Thiamine metabolism
Glutathione metabolism
Folate biosynthesis
Drug metabolism - other enzymes
One carbon pool by folate
Porphyrin and chlorophyll metabolism
Control
NCT
2
1
0
-1
-2
c
SPI1 (14g)
IRF4 (18g)
KLF13 (10g)
STAT3 (10g)
YY1_extended (16g)
BCLAF1_extended (14g)
PBX1 (13g)
TBL1XR1_extended (12g)
MAFF (11g)
HLF_extended (12g)
TFCP2L1_extended (27g)
NKX2-1 (23g)
FOXA2 (11g)
MEF2C (61g)
TCF21_extended (24g)
NFIA (15g)
RAD21_extended (18g)
STAT2 (83g)
STAT1 (118g)
IRF7 (71g)
NUAK1 (45g)
CREB3L1_extended (16g)
REL (37g)
IKZF1_extended (59g)
RUNX3 (74g)
ATF3 (10g)
IRF1 (29g)
MAFB_extended (30g)
SNAI1 (14g)
CEBPB (134g)
JUNB_extended (144g)
FOS_extended (106g)
JUND (75g)
FOSB_extended (101g)
EGR1 (112g)
0
4
5
2
9
8
1
6
3
7
3
2
1
0
-1
-2
-3

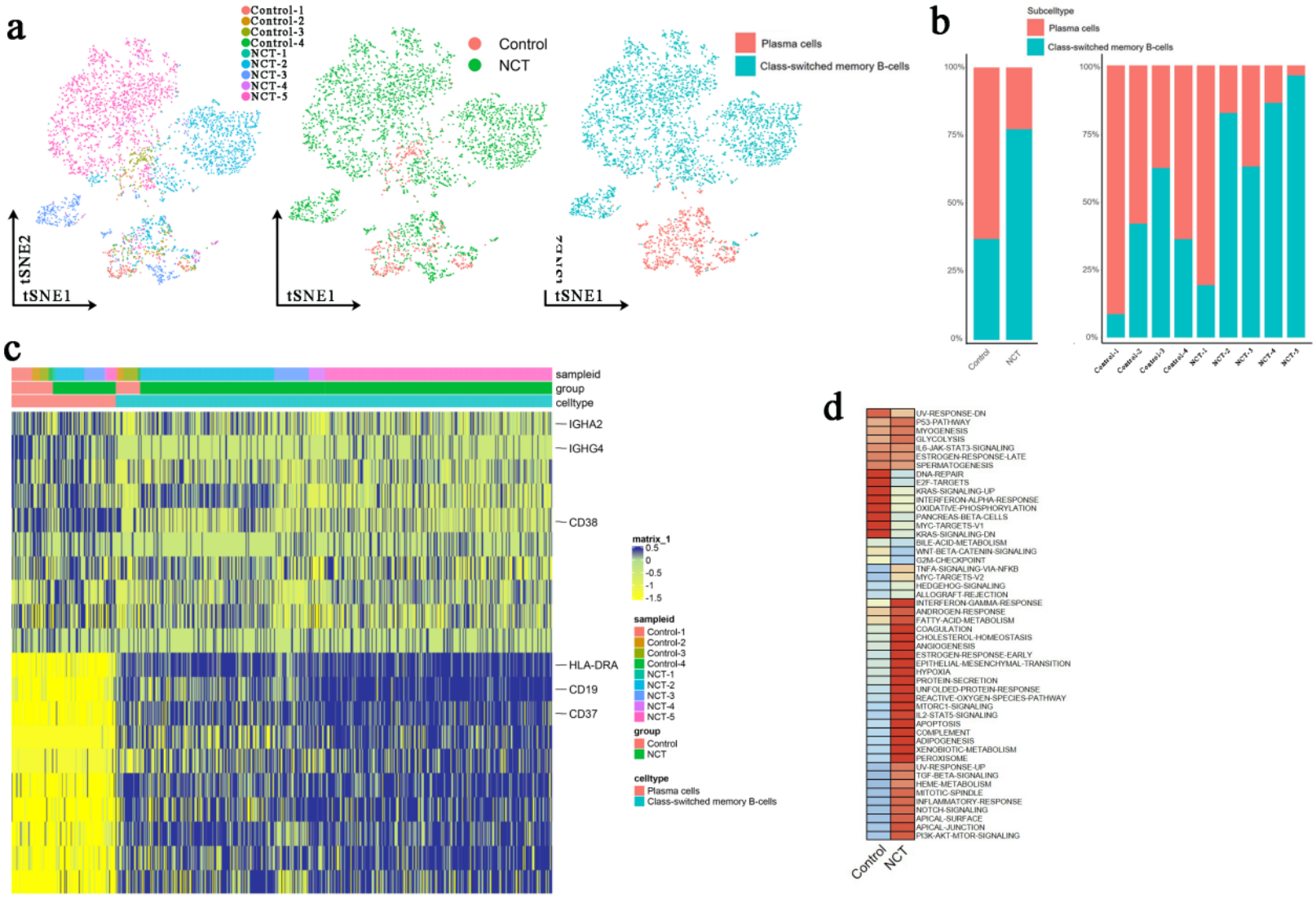
a
Control-1
Control-2
Control-3
Control-4
NCT-1
NCT-2
NCT-3
NCT-4
NCT-5
Control
NCT
Plasma cells
Class-switched memory B-cells
tSNE2
tSNE1
b
Subcelltype
Plasma cells
Class-switched memory B-cells
100%
75%
50%
25%
0%
Control
NCT
c
sampleid
group
celltype
IGHA2
IGHG4
CD38
HLA-DRA
CD19
CD37
matrix_1
0.5
0
-0.5
-1
-1.5
sampleid
Control-1
Control-2
Control-3
Control-4
NCT-1
NCT-2
NCT-3
NCT-4
NCT-5
group
Control
NCT
celltype
Plasma cells
Class-switched memory B-cells
d
UV-RESPONSE-DN
P53-PATHWAY
MYOGENESIS
GLYCOLYSIS
IL6-JAK-STAT3-SIGNALING
ESTROGEN-RESPONSE-LATE
SPERMATOGENESIS
DNA-REPAIR
E2F-TARGETS
KRAS-SIGNALING-UP
INTERFERON-ALPHA-RESPONSE
OXIDATIVE-PHOSPHORYLATION
PANCREAS-BETA-CELLS
MYC-TARGETS-V1
KRAS-SIGNALING-DN
BILE-ACID-METABOLISM
WNT-BETA-CATENIN-SIGNALING
G2M-CHECKPOINT
TNFA-SIGNALING-VIA-NFKB
MYC-TARGETS-V2
HEDGEHOG-SIGNALING
ALLOGRAFT-REJECTION
INTERFERON-GAMMA-RESPONSE
ANDROGEN-RESPONSE
FATTY-ACID-METABOLISM
COAGULATION
CHOLESTEROL-HOMEOSTASIS
ANGIOGENESIS
ESTROGEN-RESPONSE-EARLY
EPITHELIAL-MESENCHYMAL-TRANSITION
HYPOXIA
PROTEIN-SECRETION
UNFOLDED-PROTEIN-RESPONSE
REACTIVE-OXYGEN-SPECIES-PATHWAY
MTORC1-SIGNALING
IL2-STAT5-SIGNALING
APOPTOSIS
COMPLEMENT
ADIPOGENESIS
XENOBIOTIC-METABOLISM
PEROXISOME
UV-RESPONSE-UP
TGF-BETA-SIGNALING
HEME-METABOLISM
MITOTIC-SPINDLE
INFLAMMATORY-RESPONSE
NOTCH-SIGNALING
APICAL-SURFACE
APICAL-JUNCTION
PI3K-AKT-MTOR-SIGNALING
Control
NCT

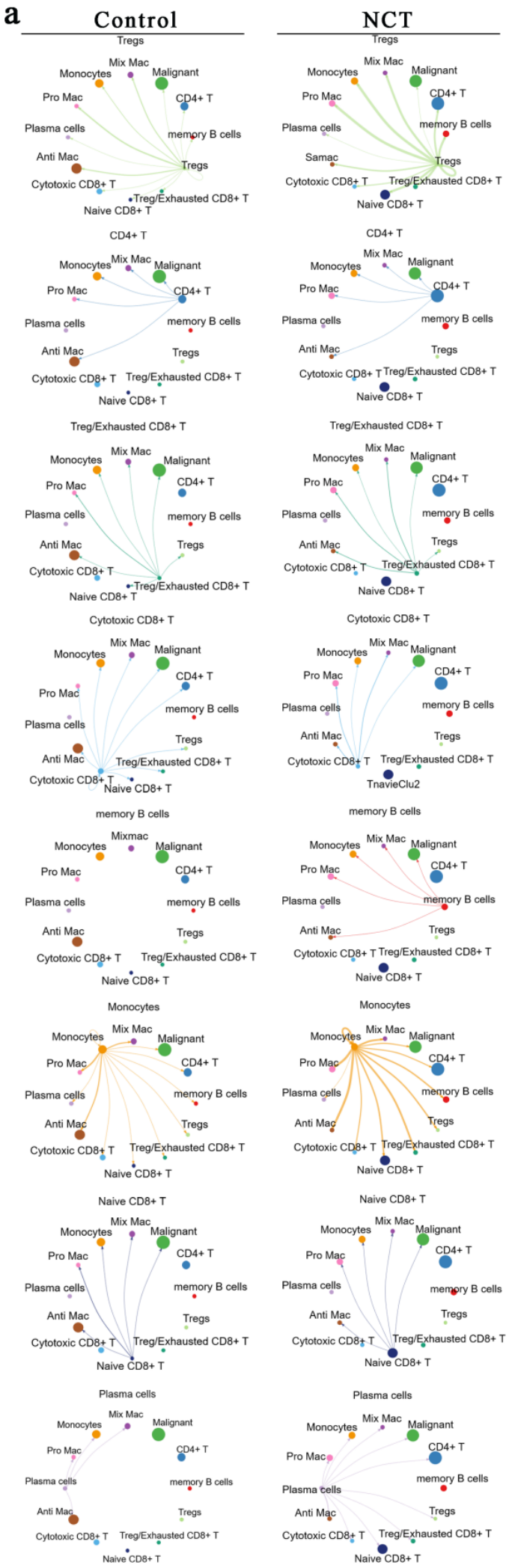
a
Control
NCT
Tregs
Mix Mac
Monocytes
Malignant
Pro Mac
CD4+ T
Plasma cells
memory B cells
Anti Mac
Tregs
Cytotoxic CD8+ T
Treg/Exhausted CD8+ T
Naive CD8+ T
Samac
TnavieClu2
Mixmac

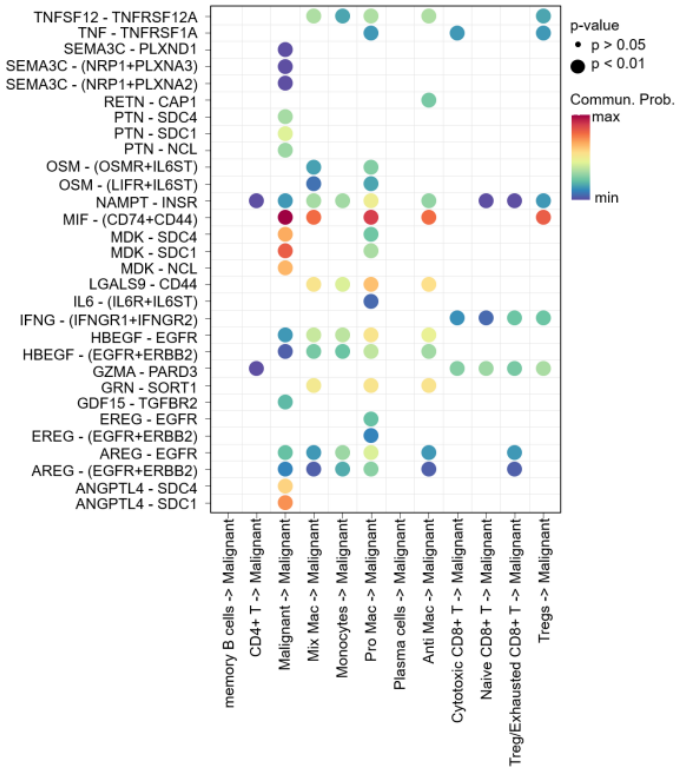
b
TNFSF12 - TNFRSF12A
TNF - TNFRSF1A
SEMA3C - PLXND1
SEMA3C - (NRP1+PLXNA3)
SEMA3C - (NRP1+PLXNA2)
RETN - CAP1
PTN - SDC4
PTN - SDC1
PTN - NCL
OSM - (OSMR+IL6ST)
OSM - (LIFR+IL6ST)
NAMPT - INSR
MIF - (CD74+CD44)
MDK - SDC4
MDK - SDC1
MDK - NCL
LGALS9 - CD44
IL6 - (IL6R+IL6ST)
IFNG - (IFNGR1+IFNGR2)
HBEGF - EGFR
HBEGF - (EGFR+ERBB2)
GZMA - PARD3
GRN - SORT1
GDF15 - TGFBR2
EREG - EGFR
EREG - (EGFR+ERBB2)
AREG - EGFR
AREG - (EGFR+ERBB2)
ANGPTL4 - SDC4
ANGPTL4 - SDC1
memory B cells -> Malignant
CD4+ T -> Malignant
Malignant -> Malignant
Mix Mac -> Malignant
Monocytes -> Malignant
Pro Mac -> Malignant
Plasma cells -> Malignant
Anti Mac -> Malignant
Cytotoxic CD8+ T -> Malignant
Naive CD8+ T -> Malignant
Treg/Exhausted CD8+ T -> Malignant
Tregs -> Malignant
p-value
p > 0.05
p < 0.01
Commun. Prob.
max
min

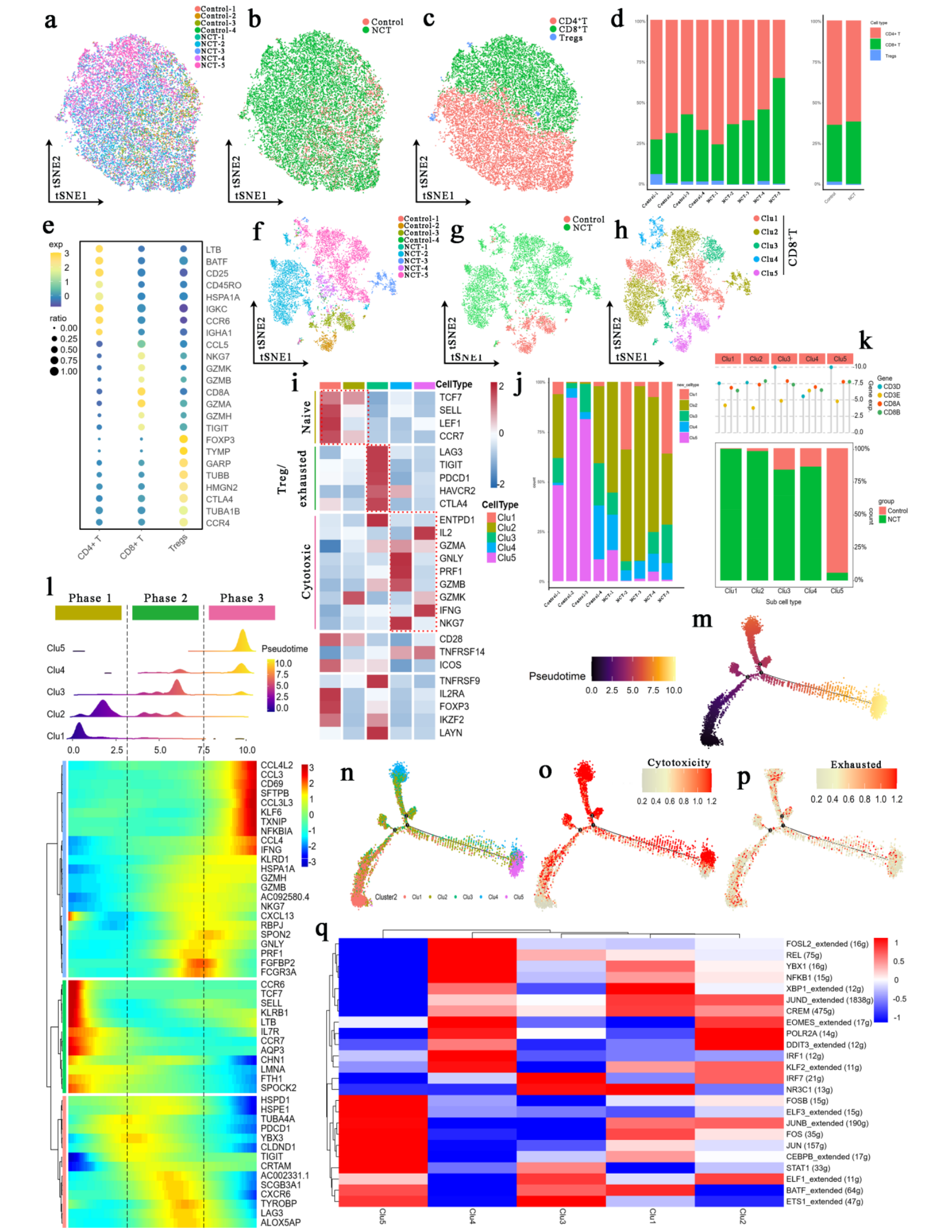
a
Control-1
Control-2
Control-3
Control-4
NCT-1
NCT-2
NCT-3
NCT-4
NCT-5
tSNE2
tSNE1
b
Control
NCT
c
CD4+T
CD8+T
Tregs
d
Cell type
CD4+ T
CD8+ T
Tregs
e
exp
ratio
LTB
BATF
CD25
CD45RO
HSPA1A
IGKC
CCR6
IGHA1
CCL5
NKG7
GZMK
GZMB
CD8A
GZMA
GZMH
TIGIT
FOXP3
TYMP
GARP
TUBB
HMGN2
CTLA4
TUBA1B
CCR4
CD4+ T
CD8+ T
Tregs
f
g
h
Clu1
Clu2
Clu3
Clu4
Clu5
CD8+T
i
CellType
Naive
Treg/ exhausted
Cytotoxic
TCF7
SELL
LEF1
CCR7
LAG3
TIGIT
PDCD1
HAVCR2
CTLA4
ENTPD1
IL2
GZMA
GNLY
PRF1
GZMB
GZMK
IFNG
NKG7
CD28
TNFRSF14
ICOS
TNFRSF9
IL2RA
FOXP3
IKZF2
LAYN
j
new_celltype
count
k
Gene
CD3D
CD3E
CD8A
CD8B
Gene exp.
group
Control
NCT
Sub cell type
l
Phase 1
Phase 2
Phase 3
Pseudotime
m
Pseudotime
n
Cluster2
o
Cytotoxicity
p
Exhausted
q
FOSL2_extended (16g)
REL (75g)
YBX1 (16g)
NFKB1 (15g)
XBP1_extended (12g)
JUND_extended (1838g)
CREM (475g)
EOMES_extended (17g)
POLR2A (14g)
DDIT3_extended (12g)
IRF1 (12g)
KLF2_extended (11g)
IRF7 (21g)
NR3C1 (13g)
FOSB (15g)
ELF3_extended (15g)
JUNB_extended (190g)
FOS (35g)
JUN (157g)
CEBPB_extended (17g)
STAT1 (33g)
ELF1_extended (11g)
BATF_extended (64g)
ETS1_extended (47g)
Clu5
Clu4
Clu3
Clu1
Clu2

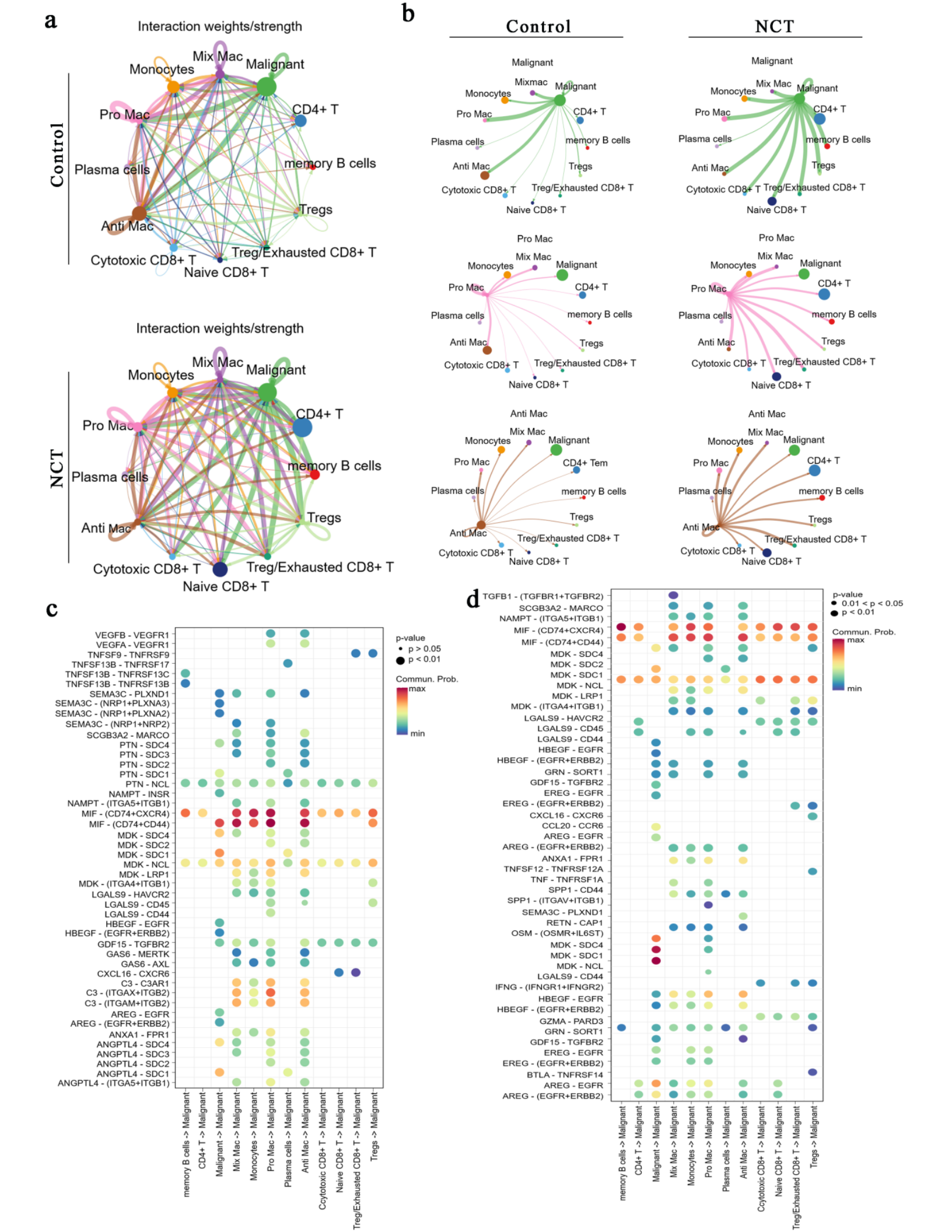
a
Interaction weights/strength
Control
Mix Mac
Monocytes
Malignant
Pro Mac
CD4+ T
Plasma cells
memory B cells
Anti Mac
Tregs
Cytotoxic CD8+ T
Treg/Exhausted CD8+ T
Naive CD8+ T
Interaction weights/strength
NCT
Mix Mac
Monocytes
Malignant
Pro Mac
CD4+ T
Plasma cells
memory B cells
Anti Mac
Tregs
Cytotoxic CD8+ T
Treg/Exhausted CD8+ T
Naive CD8+ T
b
Control
NCT
Malignant
Mixmac
Monocytes
Malignant
Pro Mac
CD4+ T
Plasma cells
memory B cells
Anti Mac
Tregs
Cytotoxic CD8+ T
Treg/Exhausted CD8+ T
Naive CD8+ T
Malignant
Mix Mac
Monocytes
Malignant
Pro Mac
CD4+ T
Plasma cells
memory B cells
Anti Mac
Tregs
Cytotoxic CD8+ T
Treg/Exhausted CD8+ T
Naive CD8+ T
Pro Mac
Mix Mac
Monocytes
Malignant
Pro Mac
CD4+ T
Plasma cells
memory B cells
Anti Mac
Tregs
Cytotoxic CD8+ T
Treg/Exhausted CD8+ T
Naive CD8+ T
Pro Mac
Mix Mac
Monocytes
Malignant
Pro Mac
CD4+ T
Plasma cells
memory B cells
Anti Mac
Tregs
Cytotoxic CD8+ T
Treg/Exhausted CD8+ T
Naive CD8+ T
Anti Mac
Mix Mac
Monocytes
Malignant
Pro Mac
CD4+ Tem
Plasma cells
memory B cells
Tregs
Anti Mac
Treg/Exhausted CD8+ T
Cytotoxic CD8+ T
Naive CD8+ T
Anti Mac
Mix Mac
Monocytes
Malignant
Pro Mac
CD4+ T
Plasma cells
memory B cells
Tregs
Anti Mac
Treg/Exhausted CD8+ T
Cytotoxic CD8+ T
Naive CD8+ T
c
VEGFB - VEGFR1
VEGFA - VEGFR1
TNFSF9 - TNFRSF9
TNFSF13B - TNFRSF17
TNFSF13B - TNFRSF13C
TNFSF13B - TNFRSF13B
SEMA3C - PLXND1
SEMA3C - (NRP1+PLXNA3)
SEMA3C - (NRP1+PLXNA2)
SEMA3C - (NRP1+NRP2)
SCGB3A2 - MARCO
PTN - SDC4
PTN - SDC3
PTN - SDC2
PTN - SDC1
PTN - NCL
NAMPT - INSR
NAMPT - (ITGA5+ITGB1)
MIF - (CD74+CXCR4)
MIF - (CD74+CD44)
MDK - SDC4
MDK - SDC2
MDK - SDC1
MDK - NCL
MDK - LRP1
MDK - (ITGA4+ITGB1)
LGALS9 - HAVCR2
LGALS9 - CD45
LGALS9 - CD44
HBEGF - EGFR
HBEGF - (EGFR+ERBB2)
GDF15 - TGFBR2
GAS6 - MERTK
GAS6 - AXL
CXCL16 - CXCR6
C3 - C3AR1
C3 - (ITGAX+ITGB2)
C3 - (ITGAM+ITGB2)
AREG - EGFR
AREG - (EGFR+ERBB2)
ANXA1 - FPR1
ANGPTL4 - SDC4
ANGPTL4 - SDC3
ANGPTL4 - SDC2
ANGPTL4 - SDC1
ANGPTL4 - (ITGA5+ITGB1)
memory B cells -> Malignant
CD4+ T -> Malignant
Malignant -> Malignant
Mix Mac -> Malignant
Monocytes -> Malignant
Pro Mac -> Malignant
Plasma cells -> Malignant
Anti Mac -> Malignant
Ccytotoxic CD8+ T -> Malignant
Naive CD8+ T -> Malignant
Treg/Exhausted CD8+ T -> Malignant
Tregs -> Malignant
p-value
p > 0.05
p < 0.01
Commun. Prob.
max
min
d
TGFB1 - (TGFBR1+TGFBR2)
SCGB3A2 - MARCO
NAMPT - (ITGA5+ITGB1)
MIF - (CD74+CXCR4)
MIF - (CD74+CD44)
MDK - SDC4
MDK - SDC2
MDK - SDC1
MDK - NCL
MDK - LRP1
MDK - (ITGA4+ITGB1)
LGALS9 - HAVCR2
LGALS9 - CD45
LGALS9 - CD44
HBEGF - EGFR
HBEGF - (EGFR+ERBB2)
GRN - SORT1
GDF15 - TGFBR2
EREG - EGFR
EREG - (EGFR+ERBB2)
CXCL16 - CXCR6
CCL20 - CCR6
AREG - EGFR
AREG - (EGFR+ERBB2)
ANXA1 - FPR1
TNFSF12 - TNFRSF12A
TNF - TNFRSF1A
SPP1 - CD44
SPP1 - (ITGAV+ITGB1)
SEMA3C - PLXND1
RETN - CAP1
OSM - (OSMR+IL6ST)
MDK - SDC4
MDK - SDC1
MDK - NCL
LGALS9 - CD44
IFNG - (IFNGR1+IFNGR2)
HBEGF - EGFR
HBEGF - (EGFR+ERBB2)
GZMA - PARD3
GRN - SORT1
GDF15 - TGFBR2
EREG - EGFR
EREG - (EGFR+ERBB2)
BTLA - TNFRSF14
AREG - EGFR
AREG - (EGFR+ERBB2)
memory B cells -> Malignant
CD4+ T -> Malignant
Malignant -> Malignant
Mix Mac -> Malignant
Monocytes -> Malignant
Pro Mac -> Malignant
Plasma cells -> Malignant
Anti Mac -> Malignant
Ccytotoxic CD8+ T -> Malignant
Naive CD8+ T -> Malignant
Treg/Exhausted CD8+ T -> Malignant
Tregs -> Malignant
p-value
0.01 < p < 0.05
p < 0.01
Commun. Prob.
max
min